Development of a Compact-Toroid Injection System for Field-Reversed Configuration Particle Refueling

（FRC 装置の粒子供給のための CT 入射法の開発）

January,　2017

Physics Major

Graduate School of Science and Technology

Nihon University

松本　匡史

Contents

List of Figures

Acknowledgements

The work presented in this dissertation has been supported tremendously from numerous people, whose support and guidance I am not thankful for. I would like to express my gratitude to some of people who particularly contributed to this undertaking, either as a teacher, a colleague, or a friend.

Firstly, I would like to acknowledge Professor Tsutomu Takahashi and Associate Professor Tomohiko Asai, who are my advisers in Department of physics, at Nihon University. The expressions of gratefulness should be extended to Professors for providing me an opportunity to study this research project.

Hiroshi Gota, Thomas Roche, and Travis Valentine who are staff at Tri Alpha Energy Inc., I really appreciate your help not only in studies but also in my daily life as well in the United State.

In addition, Ian Allfrey, Mark Morehouse, John Kinley, and William Waggoner, who are staff at Tri Alpha Energy Inc., I would like to thank to help my research.

I thank our shareholders for their support and trust, and all fellow TAE staff for their dedication, excellent work, and extra efforts.

This work was supported in part by the MOU as a part of research cooperation between the University of California at Irvine (School of Physical Science,

Department of Physics and Astronomy) and Nihon University (College of Science and Technology, Department of Physics).

Finally, I have to thank my parents for support throughout my life. All support they have provided me over the years was the greatest gift anyone has ever given me.

Chapter 1

Introduction

1.1 FRC Facility

Conventional nuclear fusion research has been advanced centering on particularly in the D-T reaction because the cross section is larger at low plasma temperature among many fusion fuel systems, where D is deuterium, T is tritium. This method is considered as a fuel of the ITER project [1]. The D-T reaction has a large cross section of the reaction. So the demand for the steady nuclear reaction is low and realization of the reaction itself is relatively easy. However, Tritium, which is a fuel, is a radioactive substance, neutrons still generate by the reaction between deuterium and tritium it has the problem that it is. This reaction necessitates measures to active the furnace structure, it is inevidence to become huge and complicated.

$$D + T \longrightarrow {}^{4}He + n$$

For this reason, we should aim at next generation nuclear fusion reactor with

less neutron load. Therefore, field-reversed configurations (FRCs), having high efficiency and compact magnetic field configuration satisfying these conditions, are getting more and more attention. The FRC has many advantages such as the magnetic field utilization efficiency is close to 100% and the reaction product can be directly used for power generation. Also, FRC's reactions, D-^3He and p-^{11}B, produce less neutrons and the risk of activation is unlimitedly low. If it is feasible, it can be expected to become the most inexpensive and highly efficient nuclear fusion reactor plasma. However, it is very difficult to maintain the short confinement time and coordination, and there are many problems to realize.

$$D + {}^3He \longrightarrow {}^4He + p$$

$$p + {}^{11}B \longrightarrow 3{}^4He$$

To realize p-^{11}B reaction, Tri Alpha Energy (TAE), Inc. has been conducted to develop a FRC's fusion reactor.

The FRC device that is constructed at TAE is the largest device in the world [6, 7]. Figure 1.1 shows a schematic layout of FRC device. This device consists of confinement region at the center of the device, two formation region for generating an FRC on the opposite ends of confinement vessel. The formation is adopted theta-pinch method [47]. Figure 1.2 indicates a concept of the C-2 device. The formed FRC is easily accelerated by the gradient of the magnetic field and achieved supersonic speeds (> 250 km/s). After collision (~ 100 μs) CTs merge into single FRC. The kinetic energy converts to the thermal energy after colliding and merging.

A typical FRC has instabilities, i.e., wobble motion (toroidal mode number $n = 1$) and rotation (toroidal mode number $n = 2$) [47]. The plasma guns to control an electric field outside the FRC are installed on the both end side of the formation section to stabilize the global instability of the FRC, such as wobble motion and FRC rotation [48]. Usual FRC does not have a heating mechanism, so the electron temperature is low. Hence, the resistance of the toroidal current will be increased. Therefore, the FRC decay rapidly. To heat the electron temperature, the neutral beam is employed on the TAE's FRC. Also, the neutral beams are aimed at mid-plane on the confinement chamber for heating, driving a current, and particle fueling. There are 6 NBs on the confinement vessel. The NBs are injected in an ion diamagnetic direction to drive current. The input beam energy is 15 keV, and total power in neutrals is 10+ MW, and the ion current per source is 145 A. The lifetime of the FRC is extended significantly by the neutral beam system, as shown in Fig. 1.3. Figure 1.3 shows comparison of the C-2/C-2U FRC's lifetime from the excluded-flux radius. The previous experimental device C-2, initially had no NBI or edge-biasing capabilities and produced $\sim$ 1 ms; the lifetime was limited by MHD instabilities. C-2/C-2U's FRC lifetime is dramatically extended from 1 ms to 10+ ms. This improvement indicates current drive by beams and fast particle accumulation in FRC. Hence, the TAE's FRC is called "advanced beam-driven FRC plasma [8].

The typical parameters of the C-2/C-2U device is: an external magnetic field $\sim$ 1 kG, separatrix radius $\sim$ 35 cm, FRC's length $2 - 3$ m, electron density $\sim 3 \times 10^{19}$ cm^{-3}, ion temperature $500 - 800$ eV, and electron temperature $100 - 150$

eV [8].

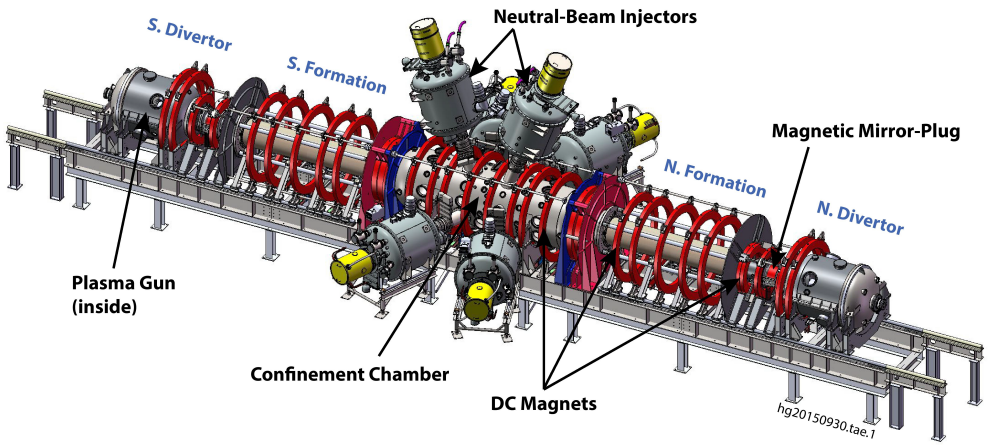

Figure 1.1. Schematic layout of C-2U machine

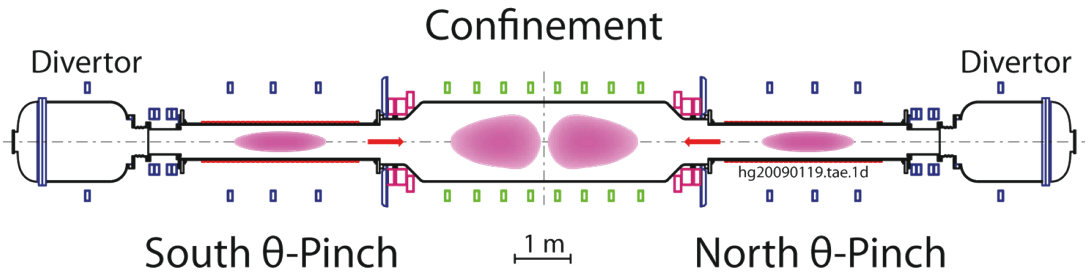

Figure 1.2. Concept of C-2/C-2U device.

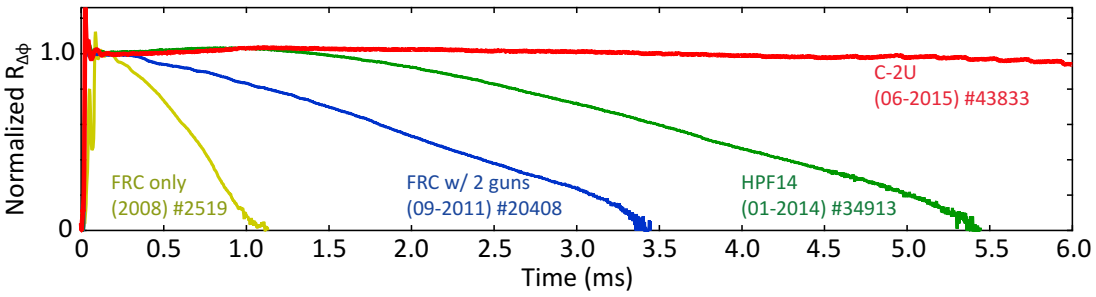

Figure 1.3. Comparison of the C-2/C-2U FRC's normalized excluded-flux radius. C-2U's FRC improved by neutral beams, guns, and wall conditioning.

1.2 Neutral Beam Heating

The core plasma needs to be heated because the temperature must achieve to self-ignition condition to maintain the plasma energy. In order to heat the plasma, joule heating can generally be used [44]. Usual tokamak plasma has a significantly large toroidal current and plasma resistivity. Therefore, the plasma will be heated by toroidal current density j and plasma resistivity η, i.e., joule heating ηj^2. However, the resistance of the plasma goes down in an inverse ratio of temperature $T^{\frac{3}{2}}$. Accordingly, the radiation loss will increase due to elevation of the electron temperature; therefore, there is a limit of joule self-heating. Thus, an additional heating technique is necessary to raise the temperature more than limits of joule heating. To elevate the temperature, a neutral beam injection (NBI) is adopted usual [37,39]. As characteristics of NBI system, the neutral particles can accelerate with high energy and though collisions with plasma particles. Then, the injected particles will be ionized. The ionized particles heat the core plasma. The energetic particles will be confined by the magnetic field and ionized mainly reaction with plasma ions. The effective cross section for ionization, σ_{eff}, is given by [21, 35, 43]

$$n_e \sigma_{eff} = n_i \sigma_i + n_i \sigma_{cx} + \frac{n_e \langle \sigma_e v_e \rangle}{v_b} + \sum_j n_j \left(\sigma_{ji} + \sigma_{jcx} \right) \tag{1.1}$$

where σ_i, σ_{cx}, and σ_e are the ion impact, the charge-exchange, electron impact, respectively. n_e and n_i are the electron and ion densities in the plasma, and v_e and v_b are electron and beam velocities, respectively. The last term indicates the ionization rate by all the impurities. The beam attenuation in the direction of the

beam is given by

$$\frac{I}{I_0} = e^{-n_e \sigma_{eff} x} = e^{-x/\lambda} \tag{1.2}$$

$$\lambda = \frac{1}{n_e \sigma_{eff}} \tag{1.3}$$

The quantity λ is defined as a characteristic of the attenuation length of the beam. An approximate expression for the attenuation length λ in the range of the interest for core plasma heating with deuterium beam is defined as

$$\lambda\,(m) = 2.8 \times 10^{17} \left(\frac{E_b\,[\mathrm{keV}]}{n_e\,[\mathrm{m}^{-3}]} \right) \tag{1.4}$$

Since the attenuation length depends on the plasma density, the density should be increased to increase the collision probability. However, the fueling rate from the NB is insufficient. Hence, the particle refueling system from the exterior becomes necessary. In order to control the plasma density, we developed the particle refueling source. In the Chapter 3, the developed particle refueling source describes.

1.3 Particle Refueling Techniques

To refuel the particles into the core plasma, gas puffing, ice-pellet, and compact toroid (CT) injection has been developed on the tokamak device. The gas puffing method with supersonic is simple and can be easily constructed on the confinement vessel, which is constructed to confine the core plasma. However, this method spread a cloud of the neutral gas surround the core plasma. As a result, the core

plasma cooled. The ice-pellet injection has been achieved efficiency of 100% on the ASDEX upgrade and sthe LHD devices [22, 25]. This method makes a pellet by compressing a gas. The ice-pellet injects the solidified neutral gas into the core plasma. However, the penetrated pellet will evaporate around the outside of the core plasma. On the ITER device which is the largest tokamak device needs a 100 km/s penetration speed to inject inside the core plasma. The recent speed of the pellet is only a few km/s. Thus, it is difficult to reach the core region [31]. Due to the low temperature, both methods cool the core plasma. Thus the gas puffing and pellet injection make a hole on the core plasma surface.

To deep refuel the particle to the core plasma, Perkins emphasized dense CT injection [31]. CT injection has been demonstrated experimentally on the several tokamak devices [28,33,34] using a magnetized coaxial plasma gun (MCPG). The electrode discharge impurities due to metal originated from electrodes. However, it does not cause major problems for core plasma. Usually, the electrode is coated with tungsten to reduce the impurities. The tungsten cannot flight vehicles at high speed because of heavy. The tungsten of 10 eV has a 1.25 km/s as a velocity. Therefore, the tungsten cannot follow the ejected CT. Also, the Larmor radius of the tungsten is larger than fueling particles (H, D_2), e.g., Larmor radius of tungsten of 10 eV is 24 cm with 0.1 T. So, it is difficult to confine the tungsten inside the magnetic field as a particle source. On the result of the tokamak device, there was no longer any impurities line of the tungsten between W^{3+} and W^{27+} on the trailing plasma [33,34]. On the JFT-2M device, the validity was confirmed that the CT is able to penetrate inside the core plasma with the high magnetic field

by the soft x-ray radiation measurement [28]. As a result, the CT injection was verified and confirmed. Also, the CT's velocity on the RACE (ring acceleration experiment) device has been achieved up to 2500 km/s [17, 18, 27]. Thus, the CT injector has gathered a sufficient amount of necessary things to inject the particles. It was verified that the CT could be able to inject under the extremely high magnetic field.

1.4 Thesis Outline

This thesis has been constructed into the eight Chapters. The first Chapter describes an introduction of the world's largest FRC device, C-2/C-2U, and indicates the heating system and particle refueling system as an energy fueling on the core plasma. Chapter 2 indicates compact toroid plasma, FRC and Spheromak. Also, the structure of the FRC which is main target of this thesis describes. Chapter 3 mentions about the concept of the magnetized coaxial plasma gun, and Chapter 4 describes the designed compact toroid injector for my research. To test the developed CT injector, we constructed the test stand to research the characteristics of the ejected CT upon the transverse magnetic field. The detailed description is in Chapter 5. After the test the CT injector on the test stand, the injector is mounted on the confinement vessel of the FRC. The installation and result are mentioned in Chapter 6. Our CT injector was upgraded to improve the effect of the neutral gas after CT injection. Chapter 7 mentions about the system of the pre-ionization technique to reduce the amount of neutral gas to breakdown.

Chapter 8 is summary of a thesis.

Chapter 2

Compact Toroids

2.1 FRC and Spheromak

Compact toroids (CTs) are toroidal plasma configurations which do not have mechanical construction inside the plasma; CT devices are simple geometry and can easily control. CTs capable of being classified two models; FRC and Spheromak. Two compact toroids are illustrated in Fig. 2.1.

1. **Field-Reversed Configuration** [38, 47]

   The FRC plasma has a closed magnetic field line structure of poloidal magnetic field in the magnetic axis direction, and maintenance of coordination is maintained by this closed magnetic field line and open magnetic field lines generated by the external coil. In addition, the poloidal magnetic field occupies most of the magnetic field that is possessed, and the toroidal magnetic field is extremely small. The average $\langle\beta\rangle$ representing the utilization efficiency of the magnetic field is characterized by being close to 100%. That

is, the externally applied magnetic field could be a weak magnetic field, and it is possible to confine plasma more efficiently than other devices such as tokamak shape. Although there are several methods for generating FRC, FRTP method is generally used to generate high temperature and high density plasma.

2. **Spheromak** [5]

The Spheromak plasma possesses both magnetic fields of the poloidal toroidal magnetic field, and the average $\langle\beta\rangle$ is 0. In addition, it forms a force-free condition, and has characteristics that it confines itself, i.e., $\nabla \times \mathbf{B} = \lambda\mathbf{B}$, where, λ is an as-yet undetermined constant. Using Ampere's law, it can be expressed as

$$\mu_0\mathbf{J} = \lambda\mathbf{B} \tag{2.1}$$

This equation is showing that the configuration is force-free, i.e., $\mathbf{J} \times \mathbf{B} = \mathbf{0}$.

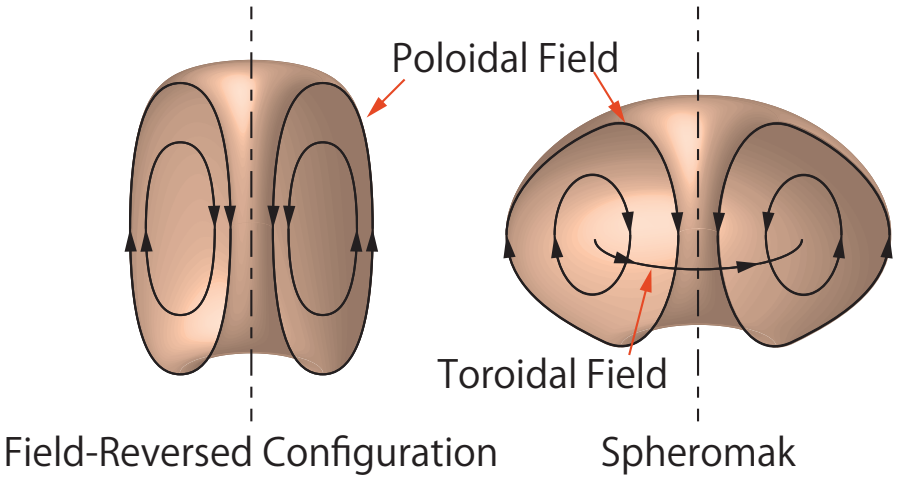

Figure 2.1. Types of the compact torus

2.2 Field-Reversed Configuration

2.2.1 Structure of FRC

Field-reversed configurations (FRCs) are constructed with open field line outside the FRC and closed field line inside the FRC. As characteristics of FRC, most of the magnetic field which is formed an FRC is a poloidal magnetic field and with no or little toroidal field. The geometrical structure of the FRC is simple, and it is shaped with cylindrical type.

Figure 2.2 shows a schematic view of an FRC. The boundary between open field line and closed field line is called separatrix. Also, the FRC's magnetic axis which is no magnetic field point is called O-point, and the cross point between the poloidal flux of FRC and machine axis is called X-point. Both points do not include a magnetic field/flux. The confinement of an FRC is maintained by the toroidal current, which flows through it on the magnetic axis inside an FRC. The confinement of an FRC is held by pressure balance of external field pressure and FRC's pressure such as magnetic and thermal. Therefore, the FRC has rotational symmetry, and it is approximated as a cylindrical shape having a simple shape.

The equilibrium of an FRC is produced by pressure balance between magnetic pressure outside the FRC and FRC's magnetic and thermal pressure. Thus pressure balance along the radial direction is defined as

$$P_{(r)} + \frac{B_{z(r)}^2}{2\mu_0} = \frac{B_e^2}{2\mu_0} \tag{2.2}$$

left term shows a FRC's pressure, and right term shows external magnetic field pressure.

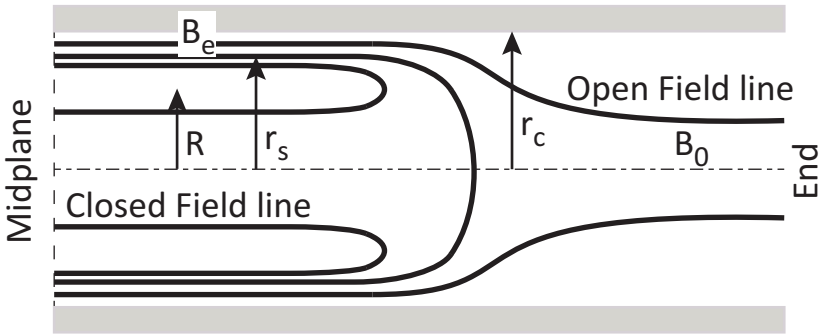

Figure 2.2. Schematic view of the field-reversed configuration.

2.2.2 Excluded Flux

When an FRC form, the distribution of the magnetic field change by separating into open and closed field line. Usually, the magnetic flux loop is assigned to measure an excluded flux. Due to form an FRC, the magnetic loop detect a fluctuation. From this relationship, the excluded flux $\Delta\Phi$ can easily represent as the diamagnetism arising from plasma presence, given by

$$\Delta\Phi = \pi r_l^2 B_e - \phi_l \tag{2.3}$$

where r_l is the radius of the flux loop , $\phi_l = \int_0^{r_l} B_e 2\pi r dr$ measured flux by the flux loop, and B_e is the external magnetic field.

2.2.3 Separatrix Radius−Formation section

A separatrix radius is one of the most important parameter. However, it cannot do directly measurement because the separatrix radius means isolation region of magnetic field. Therefore, the excluded flux measurement is also used, and the separatrix radius indirectly acquires from the excluded-flux radius. Assuming external magnetic field B_e is constant outside the separatrix, i.e., negrecting edge plasma pressure on the open field lines, the excluded flux $\Delta\Phi$ with FRC can define as

$$\Delta\Phi = \pi r_l^2 B_e - \pi(r_l^2 - r_s^2)B_e = \pi r_s^2 B_e \pi \tag{2.4}$$

where, r_s is separatrix radius. Thus, we can derive separatrix radius from magnetic field and flux measurements from magnetic probes and loops:

$$r_s = \left(\frac{\Delta\Phi}{\pi B_e}\right)^{\frac{1}{2}} = r_l\left(1 - \frac{\phi_l}{\pi r_l^2 B_e}\right)^{\frac{1}{2}} \tag{2.5}$$

With measurements from a vacuum reference, $\Delta\Phi_{vac} = \pi r_l^2 B_{e,vac} - \phi_{l,vac} = 0$, the excluded-flux radius $r_{\Delta\phi}$ is estimated as

$$r_{\Delta\phi} \simeq r_s = r_l\sqrt{1 - \frac{\phi_l}{\phi_{l,vac}}\frac{B_{e,vac}}{B_e}} \tag{2.6}$$

2.2.4 Separatrix Radius−Confinement Section

When an FRC translate from source section to confinement section, the magnetic field inside the confinement section will be excluded. However, amount of a magnetic flux does not change because a metal chamber works as a magnetic field conserver. Hence, equation 2.4 can rewrite as

$$B_0 \pi r_c^2 = B_e \left(r_c^2 - r_s^2 \right) \tag{2.7}$$

where $r_c = r_w$ is the flux conserver radius, B_0 is magnetic field on the confinement vessel before FRC translate, with the assumption that the magnetic field between the separatrix and the metal chamber B_e is uniform. Note also that the magnetic flux at the separatrix, $\Phi_s = 0$. Thus, the r_s define as

$$r_s = r_l \sqrt{1 - \frac{B_0}{B_e}} \tag{2.8}$$

2.2.5 Average Beta Relation : $\langle \beta \rangle = 1 - 1/2x_s^2$

Average beta $\langle \beta \rangle$ is one of the most important parameter of the FRC plasma. $\langle \beta \rangle$ was defined by Armstrong [2]. For pressure is written with flux function Ψ, the equation 2.2 can yield as:

$$\frac{d\Psi}{\sqrt{8}\pi \left[P_m - P_{(\Psi)} \right]^{\frac{1}{2}}} = r dr \tag{2.9}$$

The FRC has a closed field line. Hence, an integration from $r = 0$ to $r = R$ is equal to the integration from $r = R$ to $r = r_s$. Thus the magnetic axis R which is no poroidal magnetic flux is defined as;

$$R = \frac{r_s}{\sqrt{2}} \tag{2.10}$$

where,r_s is equal to $r_{\Delta\phi}$. Also, the axial pressure balance in general is given by

$$\nabla \cdot P = J \times B = -(\nabla \cdot T) \tag{2.11}$$

where P is the pressure tensor and T is the field stress tensor. Taking a surface integral and Gauss'theorem to Eq.2.11, and then Eq. 2.11 becomes

$$\frac{1}{\pi r_s^2} \int_0^{r_w} \left(\frac{P}{P_m} \right) dA = 1 - \frac{1}{2} \frac{r_s^2}{r_w^2} \tag{2.12}$$

The left hand side shows the average beta $\langle \beta \rangle$ and right hand side shows the relationship between separatrix radius and wall radius.

2.2.6 Rigid Rotor Profile

The one dimensional rigid rotor profile is used to describe the radial profile of the magnetic field and density. All theta-pinch formed FRCs usually exhibit a rigid

rotor (RR) profile, which is derived from:

$$(\nabla \times B)_\theta = -\frac{\partial B_z}{\partial r} = \mu_0 j_\theta \tag{2.13}$$

$$n_e k_B T_t + \frac{B_z^2}{2\mu_0} = \frac{B_e^2}{2\mu_0} \tag{2.14}$$

where, j_θ is toroidal current, n_e is electron density, T_t is total temperature. Assuming constant T_t, and uniform electron rotation, i.e., constant ω_e, like in a rigid rotor. Thus.

$$j_\theta = -n_e \omega_e e r \tag{2.15}$$

The solutions for density and magnetic field are given by

$$n_e = n_m \sec h^2 (K_{RR} u) \tag{2.16}$$

$$B_z = B_e \tanh (K_{RR} u) \tag{2.17}$$

where $u \equiv (r/R)^2 - 1$, $R = r_s/\sqrt{2}$ is the radius of field null ($B_z = 0$), and K_{RR} is a rigid rotor profile factor. For a typical theta-pinch FRC, $K_{RR} \leq 0.7$. Figure 2.3 shows a rigid rotor profile of magnetic field and density. A density is maximum at magnetic axis R, and the magnetic field outside the separatrix is constant.

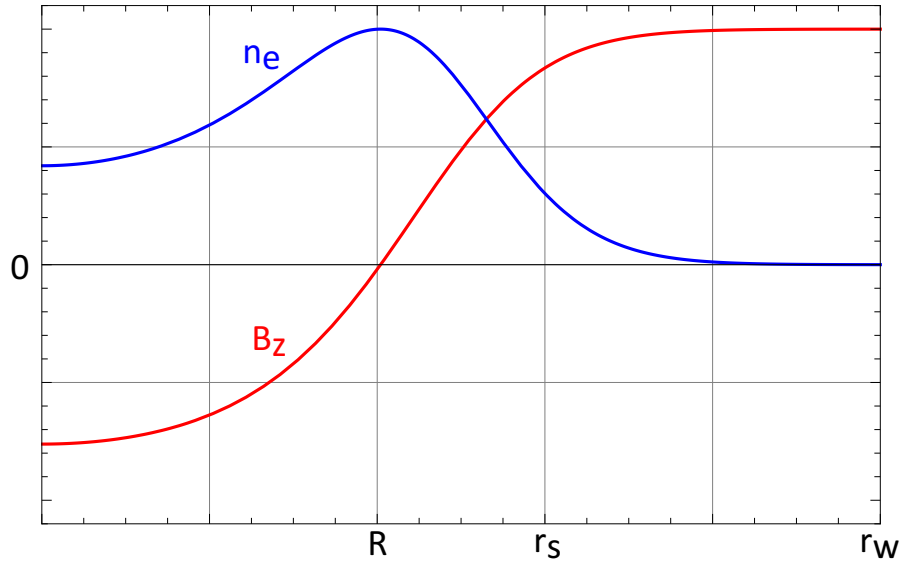

Figure 2.3. Rigid rotor profile of magnetic field and density.

2.2.7 Poloidal Flux

Poloidal flux Φ_p is defined as [2]

$$\Phi_p = \int_0^R B_z dS = \int_0^R 2\pi r B_0 \tanh K \left(\frac{r^2}{R^2} - 1\right) dr \tag{2.18}$$

$$= \pi R^2 B_e \frac{\ln(\cosh K_{RR})}{K_{RR}} \tag{2.19}$$

for $x \ll 1$, $\cosh x = 1 + \frac{x^2}{2!} + \frac{x^4}{4!} + \cdots \approx 1 + \frac{x^2}{2!}$, thus for small K_{RR},

$$\Phi_p = \pi R^2 B_e \frac{\ln(\cosh K_{RR})}{K_{RR}} \tag{2.20}$$

$$= \frac{1}{4}\pi r_s^2 B_e K_{RR} \tag{2.21}$$

Chapter 3

Concept of a Compact Toroid Injection

3.1 Magnetized Coaxial Plasma Gun

To penetrate the CT with high energy, magnetized coaxial plasma gun (MCPG) employed for particle refueling source. The inherent advantages of MCPG include (a) easily ejection of plasmoid; (b) high performance such as high density and high speed; and (c) repeatability. In addition, the CT easily adjustable performance if CT needs more kinetic energy. In this chapter, we mention about the concept of the compact toroid injector. The MCPG has a structure of coaxial cylindrical electrode and both electrodes are fixed and isolated by insulator.

In order to generate a plasma, a high voltage applies on electrodes. Usually, an outer electrode is connected to grounded potential. On the other hand, an inner electrode connects to high voltage. Also, a generated plasma needs a magnetizing to form a plasmoid. Therefore a bias coil is installed inside an inner electrode and/or outside an outer electrode. As mentioned above, a typical MCPG is constructed from coaxial cylindrical electrodes. Therefore, the distance between

electrodes is most important parameter for formation and ejection of plasmoid. To control a gun current, a MCPG need decide an inductance between electrodes. The self-inductance L of a cylindrical coaxial electrodes is as bellow:

$$L = \frac{\mu_0}{2\pi} \ln\left(\frac{b}{a}\right) \tag{3.1}$$

where, a is an outer diameter of an inner electrode; b is an inner diameter of the outer electrode.

To form a plasmoid, there are four sequences: (1) gas inlet and apply bias magnetic field, (2) breakdown between electrodes, (3) plasma accelerate by Lorentz-force, and (4) CT ejection via magnetic reconnection. Figure 3.1 shows illustrations of diagram of formation and ejection of CT from MCPG. Those main sequences are listed below in the order of process for ejection of a plasmoid from MCPG.

1. **Apply Neutral Gas and Bias Magnetic Field**

   Figure 3.1 shows an illustration about a neutral gas injects and bias magnetic field applying phases. In this figure, the bias coil inserted within an inner electrode.

   A neutral gas is enclosed inside between electrodes. Usually, a solenoid or piezo valve is adopted in order to control an amount of neutral gas. Additionally, a bias magnetic field requires magnetizing a plasma. Hence, the magnetic field applies before main discharge.

2. **Breakdown between Electrodes**

A high voltage bank is connected to electrodes with switch and triggers to generate a plasma. When switch triggered, the high voltage applies to electrodes, and then, the neutral gas is ionized. To decide a breakdown condition with neutral gas is usually used Paschen's law that is decided by pressure and distance between electrodes. The breakdown voltage is written as $V_B = f(pd)$, where p and d are pressure and distance between electrodes, respectively. In general, the Paschen's law is described as follow:

$$V_B = \frac{Bpd}{\ln(Apd) - \ln(\ln(1 + \frac{1}{\gamma}))} \tag{3.2}$$

where, A and B are constants depending on the kind of neutral gas. Also γ is secondary emission coefficient at the cathode. However, this equation is describing about the breakdown in case of parallel plate. Thus, we need reconstruct the equation from parallel plate model to cylindrical electrode model.

In the coaxial electrodes model, the electric field along the radial direction is defined as [49]

$$E = E_0 \frac{r_{in}^2}{r^2} \tag{3.3}$$

where, E_0 is a maximum electric field on the surface of inner electrode, r_{in}

is the radius of the inner electrode. The breakdown voltage can be given by

$$V_B = E_0 r_{in}^2 \left(\frac{1}{r_{in}} - \frac{1}{r_{out}} \right) \tag{3.4}$$

where, r_{out} is a inner radius of outer electrode. The maximum electric field can derive from Paschen's law. Therefore, the modified breakdown voltage V_B is derived as

$$V_B = r_{in}^2 \left(\frac{1}{r_{in}} - \frac{1}{r_{out}} \right) \frac{Ap}{\ln(pd) + B} \tag{3.5}$$

3. **Plasma Acceleration**

After switch is triggered, a radial current through between plasma. Figure 3.1(b), (c) shows appearance of the interlinkage between plasma and bias magnetic field. A gun current through an inner electrode, and then a toroidal field which is circumferential direction occurs behind the plasma. The plasma receives a Lorentz-self force $\mathbf{J} \times \mathbf{B}$, where, $\mathbf{J}$ is gun current and $\mathbf{B}$ is toroidal magnetic field which is generated from gun current.

4. **CT Ejection**

The interlinked plasma capture a toroidal field and poloidal field. After ejection from the MCPG, the magnetic reconnection occurs at the region of the radial field of bias magnetic field. Due to reconnection, the plasmoid will be separated from MCPG. At this time, the plasma receives force of drag of bias magnetic field. To estimate that drag force, the relationship between

circuit energy and magnetic energy uses as bellow.

$$F = \frac{1}{2} L_{gun} I_{gun}^2 - \frac{B_{bias}^2}{2\mu_0} \pi a^2 \tag{3.6}$$

where, L_{gun} is inductance of electrode, I_{gun} is gun (discharge) current, and B_{bias} is a magnetic field within the electrodes. This equation shows theoretical model. Also the ejection condition such as relationship of ejection between machine design and gun current for ejection CT from MCPG is determined experimentally [3]. The requirements for ejection is that the magnetic pressure of generate by gun current such as gun current must be higher than drag force of the bias magnetic field. The relationship is written as follow:

$$\lambda_g = \frac{\mu_0 I_{gun}}{\Psi_{bias}} \geq \lambda_c \tag{3.7}$$

where, Ψ_{bias} is magnetic flux of a bias coil, and λ_c is a limit against which is determined by machine geometry. The threshold λ_c is found experimentally by Barnes and Brown [4, 9], the value of the threshold is indicated as $\lambda_c = \pi/\Delta d$, where, Δd is distance of the electrodes. From this relation, Eq. 3.7 is rewritten as

$$\frac{\mu_0 I_{gun}}{\Psi_{bias}} \geq \frac{\pi}{\Delta d} \tag{3.8}$$

This equation is used to decide the electrodes design such as diameter and

electrode interval between inner and outer electrode. Then, gun current and amount of magnetic flux is determined by construction of the designed electrodes.

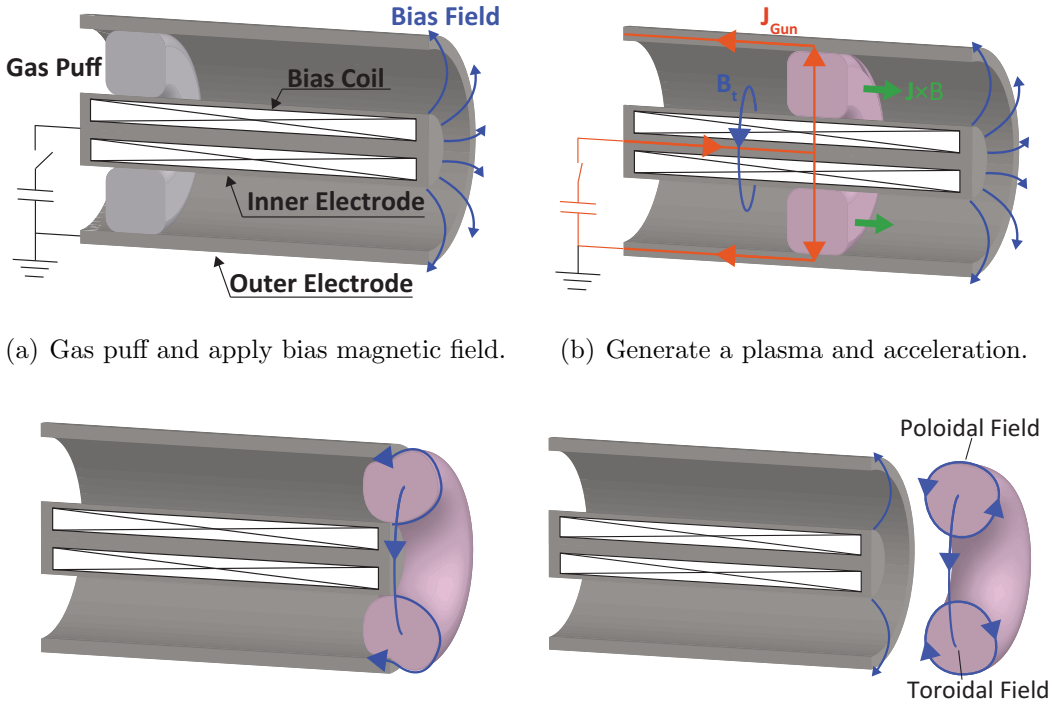

(a) Gas puff and apply bias magnetic field.

(b) Generate a plasma and acceleration.

(c) Bias field captures accelerated plasma.

(d) Reconnection and ejection

Figure 3.1. Illustration of diagram of formation and ejection of CT from MCPG.

3.2 Magnetic Tension by Transverse Magnetic Field

A CT model of trajectory inside confinement vessel has been employed the conducting spherical model, which is a perfectly conducting model, so far, to estimate the penetration depth [34, 42]. The kinetic energy density must be exceeded by

the magnetic field energy density:

$$\frac{d}{dt}\int_{CT}\frac{1}{2}\rho v^2 dV \geq \frac{d}{dt}\int_{CT}\frac{1}{2\mu_0}B^2 dV \tag{3.9}$$

where ρ, v, and B are the CT density, CT velocity, and magnetic field of CT passage, respectively. To estimate the initial condition of the CT, taking $v = v_{ct}$ and $B = 0$ as a initial condition, and $v = 0$ and $B = B_{target}$ as a final condition, so the initial kinetic energy of the the penetrated CT can derive from Eq.(3.9):

$$\frac{1}{2}\rho {v_{ct}}^2 V_{CT} \geq \frac{1}{2\mu_0}B_{target}^2 V_{CT} \tag{3.10}$$

where V_{CT} is CT volume. From this equation, the required energy can estimate. The required energy of C-2/C-2U is 4 kJ/m^3, so the velocity and density of the CT are; velocity 70 km/s and density 1.0×10^{21} m^{-3}. Furthermore a equation of motion of the CT can derive from Eq.(3.9) by taking z-axis along the CT direction. The equation as follows [40–42]:

$$\frac{d}{dt}\int_{CT}\frac{1}{2}\rho v_z^2 dV \geq \int_{CT} -\frac{\partial z}{\partial t}\frac{\partial}{\partial z}\frac{1}{2\mu_0}B^2 dV \tag{3.11}$$

$$\frac{\partial}{\partial t}\rho v_z = F - \frac{\partial}{\partial z}\frac{B^2}{2\mu_0} \tag{3.12}$$

where F is the CT acceleration force. The magnetic pressure at the second term affect the CT as deceleration. However, an actual CT has a current profile. So

the Lorentz force $\boldsymbol{J} \times \boldsymbol{B}$ acts between magnetic field of the target plasma and CT. The Lorentz force consists of the magnetic field pressure and the magnetic field tension force:

$$\boldsymbol{J} \times \boldsymbol{B} = -\nabla \left(\frac{B^2}{2\mu_0} \right) + \frac{(\boldsymbol{B} \cdot \nabla)\, \boldsymbol{B}}{\mu_0} \tag{3.13}$$

Thus, the CT's velocity is reduced not only by magnetic pressure but also by magnetic tension of the external field. Therefore, the equation of motion for CT which include a term of effect of magnetic field is represented as,

$$\frac{\partial}{\partial t} \rho \boldsymbol{v} = \boldsymbol{F} - \nabla \left(\frac{\boldsymbol{B}^{\,2}}{2\mu_0} \right) + \frac{(\boldsymbol{B} \cdot \nabla)\, \boldsymbol{B}}{\mu_0} \tag{3.14}$$

Chapter 4

Designed CT Injector System

The CT injector system has been developed for the Tokamaks. These CT injectors have a formation section and an acceleration section. Firstly, the initial CT generates on the formation section, and then CT accelerates on the acceleration section to ramp up a kinetic energy due to target magnetic field has over 1 T [17,18,27,28,31,33,34]. The accelerated CT is easily achieved to a few hundred km/s. On the RACE experiment, the velocity achieved to 2500 km/s. Additionally, the CT was penetrated and reached to core region of the core plasma.

The designed CT injector developed for the C-2/C-2U FRCs. When the CT injector for C-2 FRC developed, the electrode's distance decides from Tokamak's CT injector design as a reference. However, the external magnetic field for a confinement of C-2 FRC is only 0.1 T. Hence the kinetic energy is much smaller than Tokamak's CT injector. Furthermore, the CT injector does not need acceleration section because the typical MCPG easily reach 100 km/s. Therefore, our designed CT injector decided a model without acceleration system. To reach high speed, 100 km/s, we adopted 125 μF of capacitor bank and applied 10 kV to through the

high current. As a result, the gun current achieved 190 kA. Hence, the CT can quickly eject through the bias magnetic field. Additionally, the gas puff system can control amount of neutral gas. Hereby, the CT's kinetic energy available to control, e.g., low density with high speed, and high density with slow speed. Additionally, the multi-pulse system developed for the multi-pulse CT injection with high frequency. This system charge two banks in parallel, and then these banks can discharge independently. Furthermore, we employed a conducting shell to control an initial breakdown by trapping a bias magnetic field between electrodes. Then the $E \times B$ drift occurred and an electron starts a drift motion. Thus, the breakdown timing can control easily due to generate a plasma before breakdown.

In this chapter, the system of the CT injector will be described and mentioned. The design of the CT injector describe in section 4.1. In the section 4.2, the repetition system of the CT injection describe a circuit. In section 4.3, it is described about the conducting shell method.

4.1 Schematic of the Developed CT Injector

4.1.1 Design of the CT Injector

The MCPG, newly designed for C-2 FRCs, had been developed [26]. Figure 4.1 shows the schematic illustration of the recent CT injector. The designed CT injector adopted MCPG, which has cylindrical coaxial electrodes. Both electrodes are connected with ceramic break at the The outer diameter of the inner electrode and inner diameter of the outer electrode are 54.0 mm and 83.1 mm, respectively.

The inductance between electrodes is 86 nH/m. Thicknesses of these electrodes are 3 mm. The stainless-steel (SS 304L) electrodes consist of inner and outer electrodes. The potentials of electrodes are the following: the inner electrode is the cathode, the outer electrode is the anode, which is grounded. The diameter of outer electrode was selected to be compatible with the available interface on the C-2 vessel.

The inner electrode discharge impurity metals from electrode. Therefore, the electrode usually coats with tungsten because of high-melting point, the effect of refractory electrode coatings is shown by Brown [10]. The surface of the inner electrode is coated with tungsten ($0.2 - 0.3$ μm in thickness) in order to reduce the production of impurities from electrode into plasmoid. This coating applied with a "Vacuum Plasma Spraying" technique. The inner electrode consists of the hemispherical head; the head replaceable with other length for extension. Furthermore, the cylindrical part has cavity where the bias coil can be inserted from the end flange.

The gas puff ports are arranged on the outer electrode. This system mention on Section 4.1.3. Also, an extension electrode is connected on the muzzle of the outer electrode where is inside the ceramic break. The role of extension electrode is; protect ceramic break from the plasma, and suppression of magnetic field diffusion which has CT.

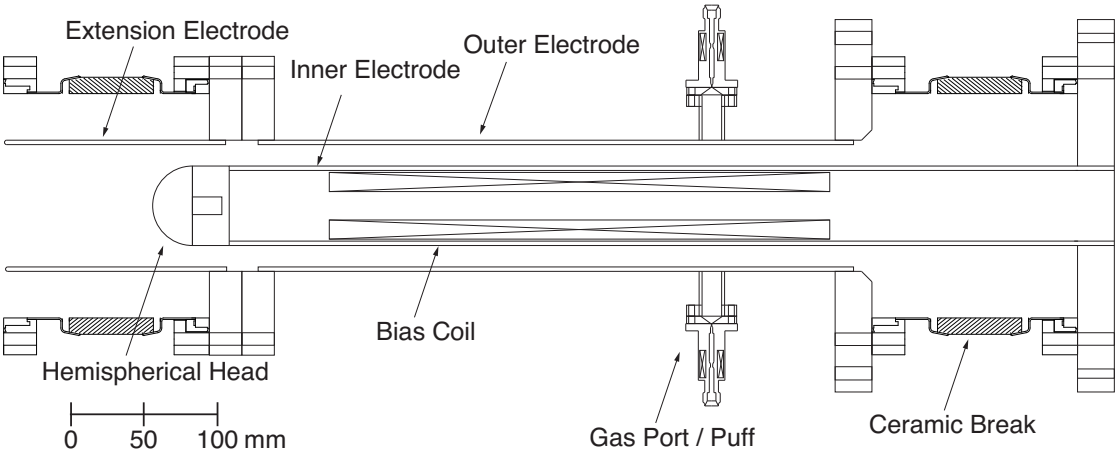

Figure 4.1. Schematic illustration of the CT injector.

4.1.2 Bias Coil System

A bias magnetic field is requires for magnetizing the plasma. The MCPG described herein has an internal bias coil, installed inside the inner electrode. Thereby, as the bias coil is not fixed to the inner electrode, the bias coil can be moved axially and can be arranged for different bias coil configurations (shorter, longer, turns, etc.). The bias coil is wound on a rod (22 mm in O.D., PVC) has 60 turns across 2 layers with inductance of approximately 20 μH turns and measures approximately 18 cm in length. The cable for the bias coil can withstand high voltages applied on the inner electrode.

The bias coil should be slower rise time because the magnetic field must penetrate through the electrode made by stainless. Figure 4.2 shows schematic diagram of the bias coil circuit. In order to make slow rise time, the electrolytic capacitor of 50 mF employed of 450 V. To rectify the bias current, the diode installed in parallel. The start switch adopted the thyristor. Due to large capacitance, the bias coil can easily modify to different type, because the frequency of the bias field

is decided mainly by capacitance.

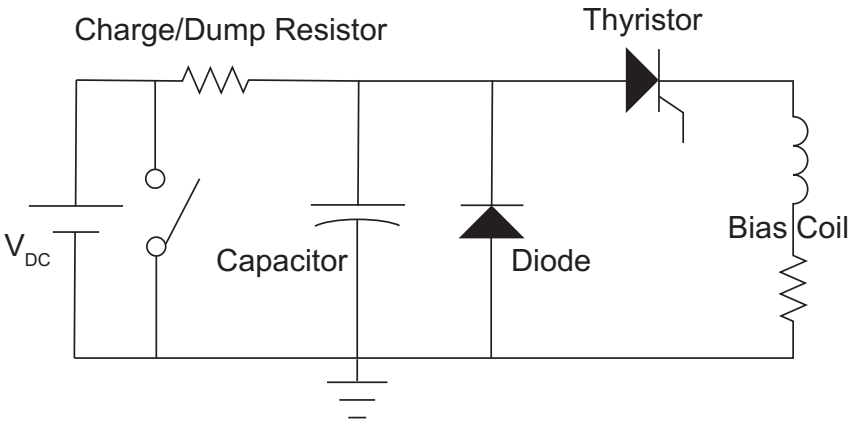

Figure 4.2. Schematic diagram of the bias coil circuit.

4.1.3 Gas Puff System

The CT injector has four ports on the outer electrode with a tangential angle in 90-degree intervals, as shown in Fig. 4.3. These pipes for the gas inlet adopted O.D. 17.3 mm and has a larger diameter and shorter length compare with the original CT injector. By using this tube, the puffed gas is diffused smoothly between electrodes. Therefore, it can control the gas flow, i.e., amount of gas inside the vacuum.

A fast solenoid valve (Parker Hannifin Corp., model: 009-0442-900) is employed to satisfy required fast-response time because the amount of gas is a critical parameter to generate a plasmoid. The puff valves are typically driven by a 28 V_{DC} pulse. In order to realize the fast response of the valve, a high-voltage short pulse is initially applied ($\sim$300 V at the peak). The gas puff driver has been employed in the series of CT injection experiments, as shown Fig. 4.4. To arbitrarily change

gas condition between electrodes, a gas injection timing and opening time of the gas puff can easily control by using this driver. Also, the gas pressure can control. Figure 4.5 shows the gas sealing amount by changing the puff duration. with 40 psia. To estimate the number of gas inlet, the background pressure and volume used.

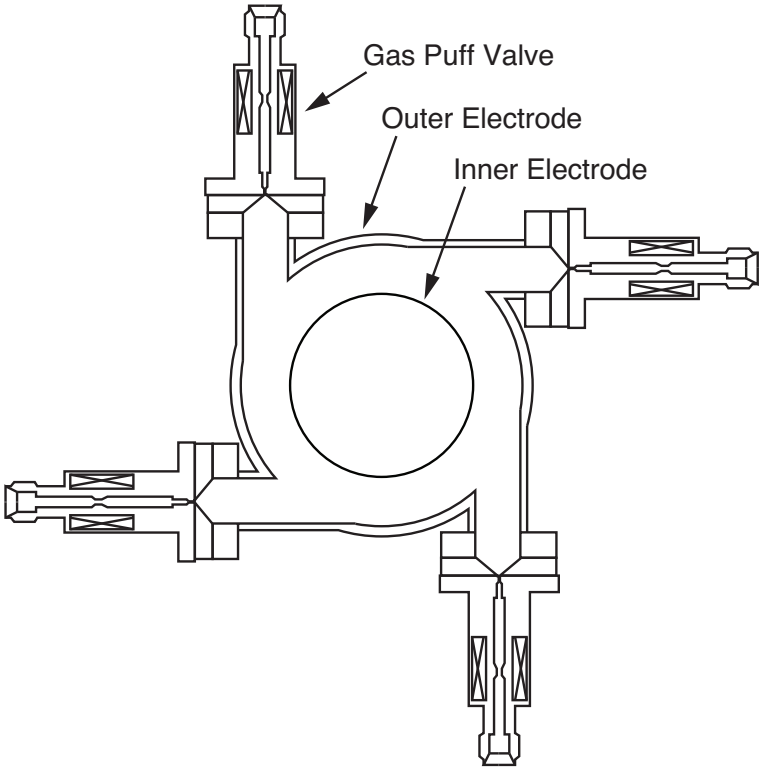

Figure 4.3. Schematic of cross section of gas puff ports

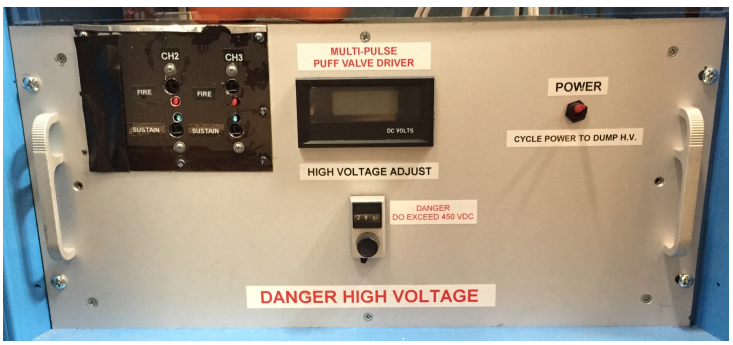

Figure 4.4. Gas puff driver made by TAE.

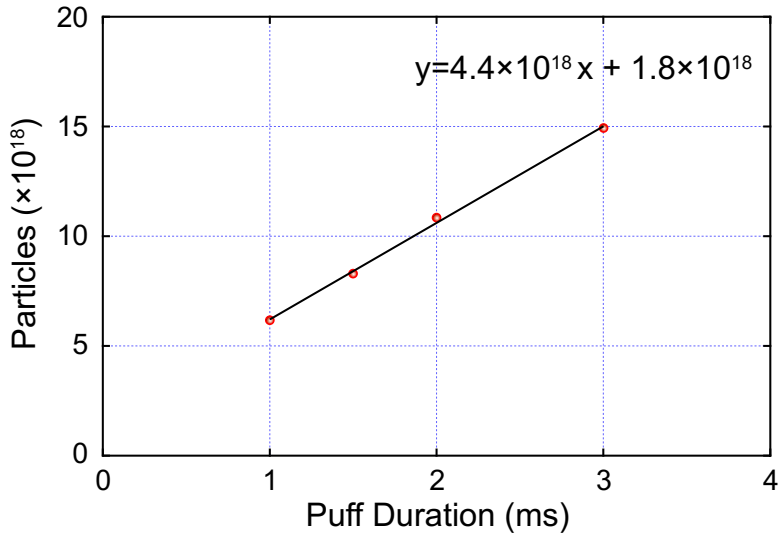

Figure 4.5. Gas sealing amount, which is estimated from different in background pressure. Background pressure was $3 - 5 \times 10^{-6}$ Torr, and Puffed pressure was 40 psia.

4.2 Repetition Circuit for Multi-Pulse CT injection

The schematic diagram of the multi-pulse circuit is shown in Fig. 4.6. Multi-pulse CT injection systems have been developed mostly for the Tokamak devices, e.g. Saskatchewan compact torus injector [29]. However, the highest repetition rate is 0.33 Hz and too slow for our projects. The lifetime of the FRC at the C-2U is only a 10 ms. In addition, the decaying rate of the particles is faster than tokamak devices. Since, the repetition speed must be more faster. Hence, we have to develop the new multi-pulse system with higher repetition rate. The developed system has short recovery time, which allows the repetition rate up to 1 kHz. This circuit is the fastest repetition rate in the world for such a system. The problem with low pressure gas switches is the clearing time for the plasma in the switch. The

multi-pulse uses a circuit similar to the single pulse power supply, but uses diodes as the crowbar and blocking element. The charging voltage is approximately 10 kV and gun current is 190 kA at the peak. Also, the rise time is 10 μs. A more detailed explanation is found in Section 5.3. The main discharge switch (start switch) used a Thyristor. The crowbar is in parallel with the capacitor in order to reduce stresses on the diode. Although the diodes have significant action ratings and high DC voltage blocking they are not immune to fast transients. Snubbing is also necessary to kill transients due to stray inductance in the circuit. Figure 4.7 shows the picture of the actual multi-pulse circuit. Green and Orange parts are resistance and capacitor for the snubber circuit, respectively.

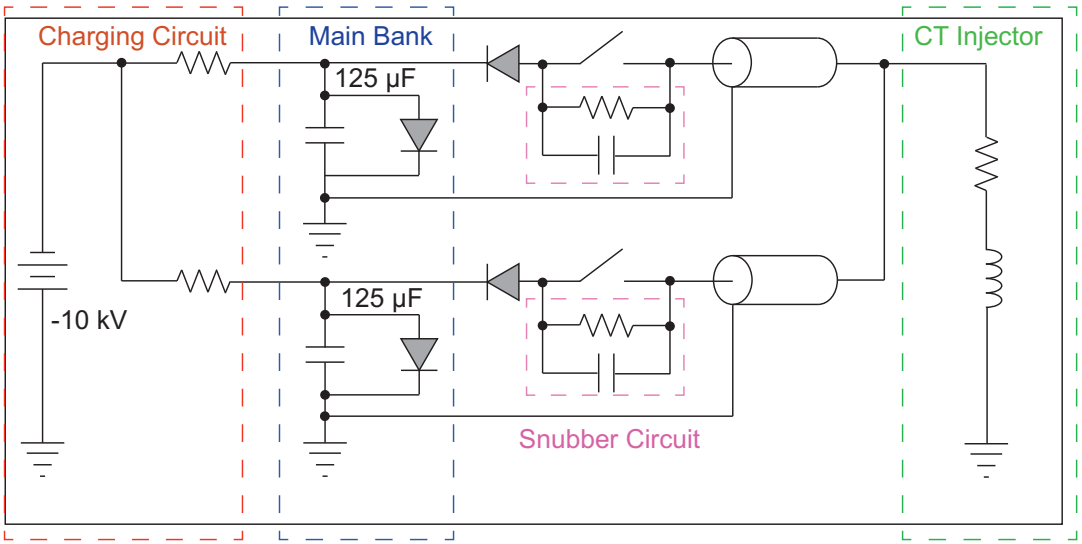

Figure 4.6. Schematic diagram of multi-pulse discharge circuit, which is include charging circuit, main bank, snubber circuit, and CT injector.

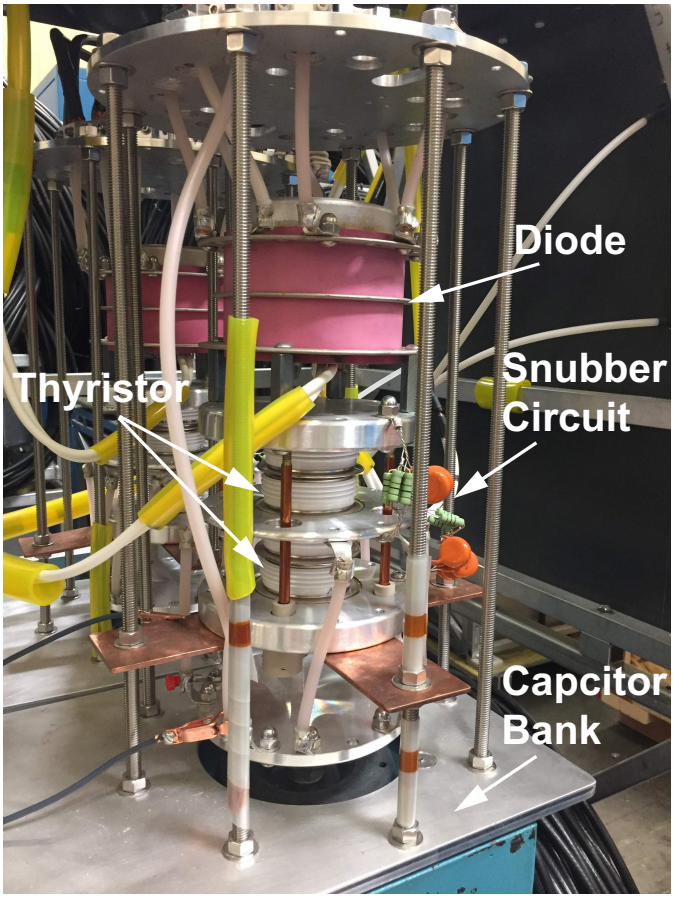

Figure 4.7. Picture of the actual multi-pulse circuit, which is including thyristor switch, diodes, and snubber circuit.

4.3 Breakdown Control by Conducting Shell

Actual breakdown process of the MCPG differs Paschen's law, i.e., a particles which is emitted from cathode rotates by $E \times B$ drift, where E is electric field of applied voltage on the electrodes, B is magnetic field from bias coil. When this motion is present, the effective pd is changed. The modified effective Paschen's law $(pd)_{eff}$ is as follows [19, 32]:

$$(pd)_{eff} = pd\sqrt{1 + \left(\frac{\Omega_e}{\nu}\right)^2} \tag{4.1}$$

where Ω_e is the electron cyclotron frequency, and ν is the collisional frequency of electron-neutral gas. As above equation, the $(pd)_{eff}$ is greater than pd of Paschen's law. Thus the magnetic field is critical parameters to control the breakdown. As shown in section 4.1, the bias coil was installed inside the inner electrode. The bias magnetic field diffuse outside of the outer electrode because a skin depth of the inner and outer electrode is same. Therefore, this system cannot efficiently utilize a magnetic field for breakdown. To control the distribution of the magnetic field, we adopted the conducting shell. The skin depth of conducting shell must be longer than material of the electrodes. The skin depth is generally well-known, it decides by resistivity of the material ρ, magnetic permeability μ, and angular frequency of current ω. The skin depth δ is

$$\delta = \sqrt{\frac{2\rho}{\omega\mu}} \tag{4.2}$$

On the our device, a copper employed. A copper has multiple characteristics; (1) it can easily processing, and (2) it has a thin skin depth: $\delta_{SS}/\delta_{Cu} \sim 6.4$.

To estimate an effect of conducting shell, the distribution of magnetic field calculated to solve an equation of magnetic diffusion. The equation can define

from Maxwell equations. The equation of magnetic diffusion is as follows:

$$\frac{\mu}{\eta}\frac{\partial B}{\partial t} = \nabla^2 B \tag{4.3}$$

where, η and μ are magnetic duffusivity and magnetic permeability, respectively. To calculate this equation, an alternative direction implicit (ADI) method used [30]. Also calculation model defined as actual designed MCPG, and bias current used as an actual waveform. Figure 4.8 shows the distribution of the magnetic field by calculation. Figure 4.8(a) shows a typical distribution of the magnetic field generated from inserted bias coil. Figure 4.8(b) shows a magnetic field distribution with conducting shell. As a calculation result, The magnetic field is trapped by conducting shell and increase the magnetic field between electrodes.

As mentioned above, collision frequency of the electron is critical parameter for breakdown, i.e., $E \times B$ drift is important. The initial electron usually emits from cathode, then it starts motion by electric field and magnetic field. If the conducting shell does not use, the magnetic field is distributed outside of the outer electrode. Therefore, the emitted electron from cathode goes to anode along the electric field. On the other hand, the conducting shell makes the axial magnetic field under the shell. By this effect, the electron starts cyclotron motion by $E \times B$ drift and extend mean free path before reach to anode. Thus the electron generates more plasma before breakdown and thus the sufficient quantity with less gas case.

Figure 4.9 shows result of comparison of breakdown between with and without conducting shell. The bias magnetic field varied to change the intensity. As a

result, the with conducting shell case was accelerated the breakdown by increasing the magnetic field.

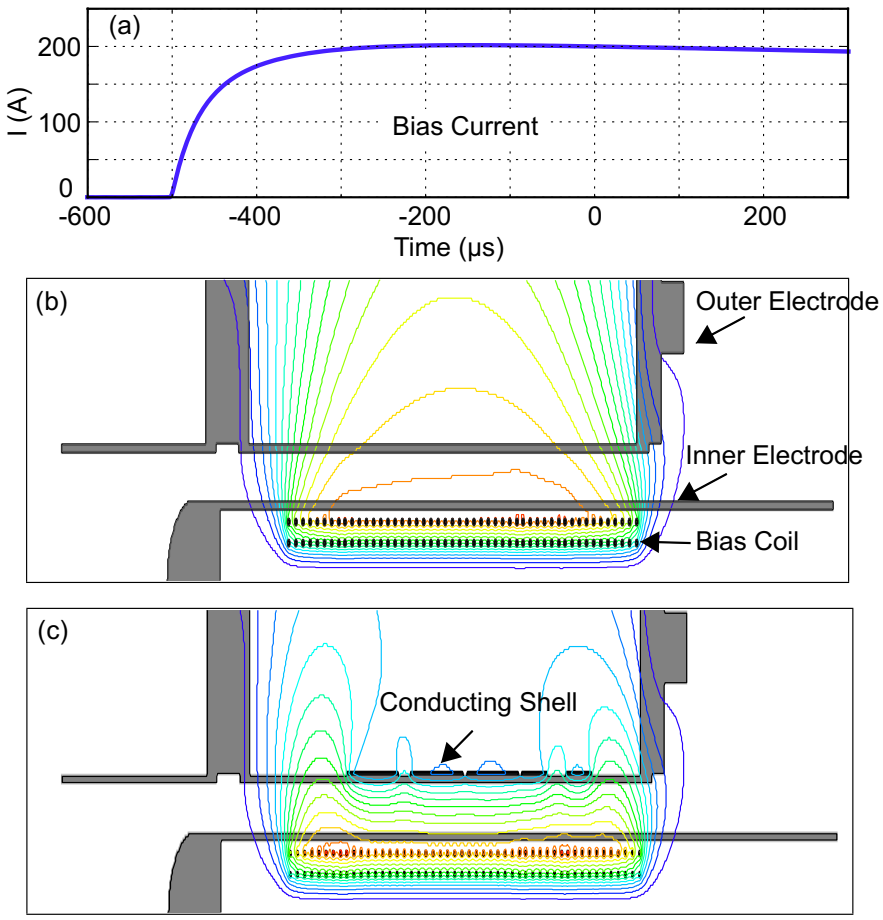

Figure 4.8. Distribution of the magnetic field from bias coil. (a) waveform of actual bias current, (b) without conducting shell at t=0, (c) with conducting shell at t=0.

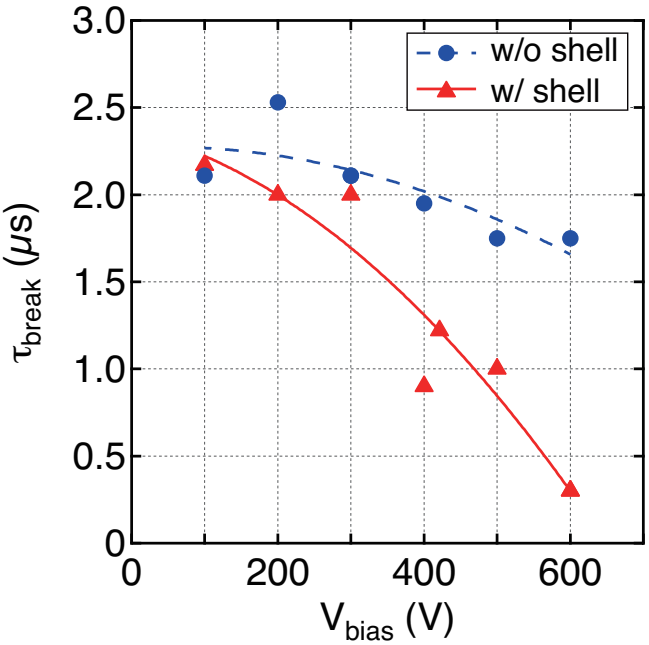

Figure 4.9. Comparison between with and without conducting shell.

Chapter 5

Characteristics Evaluation for Compact Toroid Injector

5.1 Requirement for CT Injection

As mentioned above, the C-2U FRC which is driven by NBI is dramatically extended the lifetime for over 10 ms. However, a deposited particle number from the NB is not enough to FRC. So, the FRC requires particle refueling from an external source. The CT injector which is constructed by coaxial electrode system can easily transport a large number of particles to the FRC through the external magnetic field which is surrounding the FRC. Figure 5.1 shows the time evolution of the particle loss rate with a linear approximation. the particle loss rate by linear approximation was $2.0 - 4.0 \times 10^{18}$ /ms. Therefore, the requirement parameters for the CT needs particles $> 2.0 \times 10^{18}$/ms. Also, the energy density to cross the magnetic field, the CT needs over 4 kJ/m^3. From these values, the CT's velocity can easily estimate for penetration to external field to reach the FRC. The re-

lationship between kinetic energy density and magnetic energy density is shown as Eq. 3.10. The velocity v_{ct} can estimate as $v_{ct} = \sqrt{E_m/\{m_i Particles/V_{ct}\}\,/2}$, where, E_m and mi is magnetic energy density and mass of an ion. Our device has a cylindrical pipe with a diameter of approximately 10 cm on the muzzle, and typical CT length is longer than 50 cm. Assuming that the length of the ejected CT is 50 cm and diameter of the CT is 10 cm, the velocity must be higher than 97 km/s as an indicator.

In this chapter, it describes characteristics evaluation of the CT on test stand including evaluation region for CT's parameter and trajectory measurement for the CT inside the transverse magnetic field.

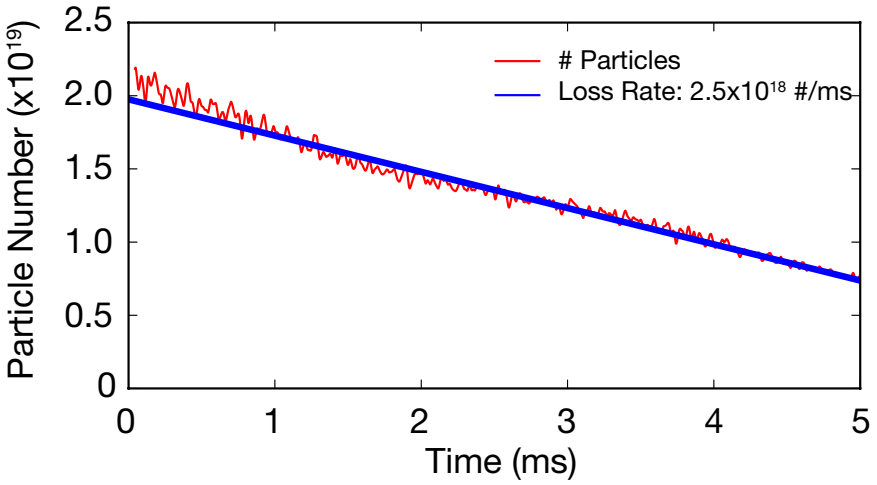

Figure 5.1. Time evolution of particle loss rate of the C-2U (Red line). Blue line shows linear approximation of particle decay late.

5.2 Schematic of the Test Stand

Figure 5.2 shows a picture of a global image of the test stand, including CT injector, drift tube, and glass tube with a transverse magnetic field. Figure 5.3 shows the

structure of the transverse coil with a square shape. In order to characterization of the plasma parameter of an ejected CT, the drift tube can use for some diagnostics. Also, the diameter of the drift tube is approximately 10 cm. Additionally, an insulator is installed between drift tube and CT injector for isolation. The glass tube is located after drift tube. The another square coil is mounted on the opposite side to generate the perpendicular field to machine axis. The role of the glass tube is to measure the behavior of the CT inside the magnetic field, which is for simulation of the axial magnetic field surrounding FRC. The glass tube also has some diagnostics for reviewing the trajectory of CT, such as magnetic diffusion of transverse field and emission from plasma.

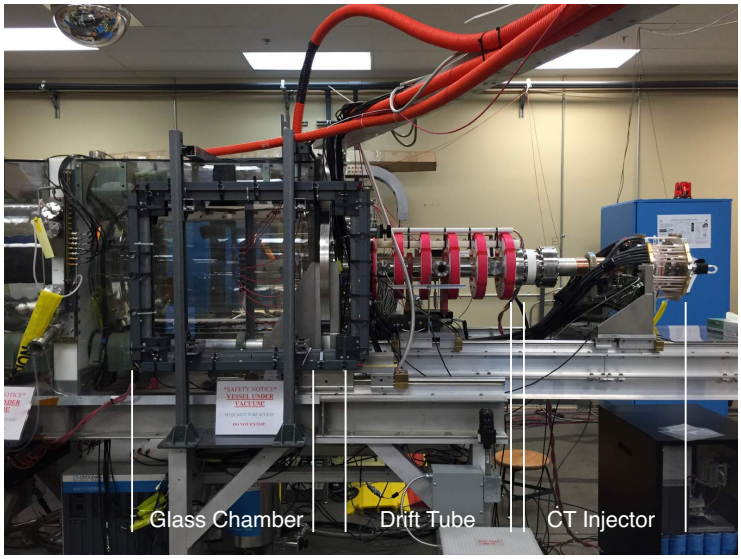

Figure 5.2. Picture of the test stand for the CT injector including CT injector, drift tube for measurement of characteristics of an ejected CT, and glass chamber to estimate a trajectory of a penetrated CT inside transverse magnetic field.

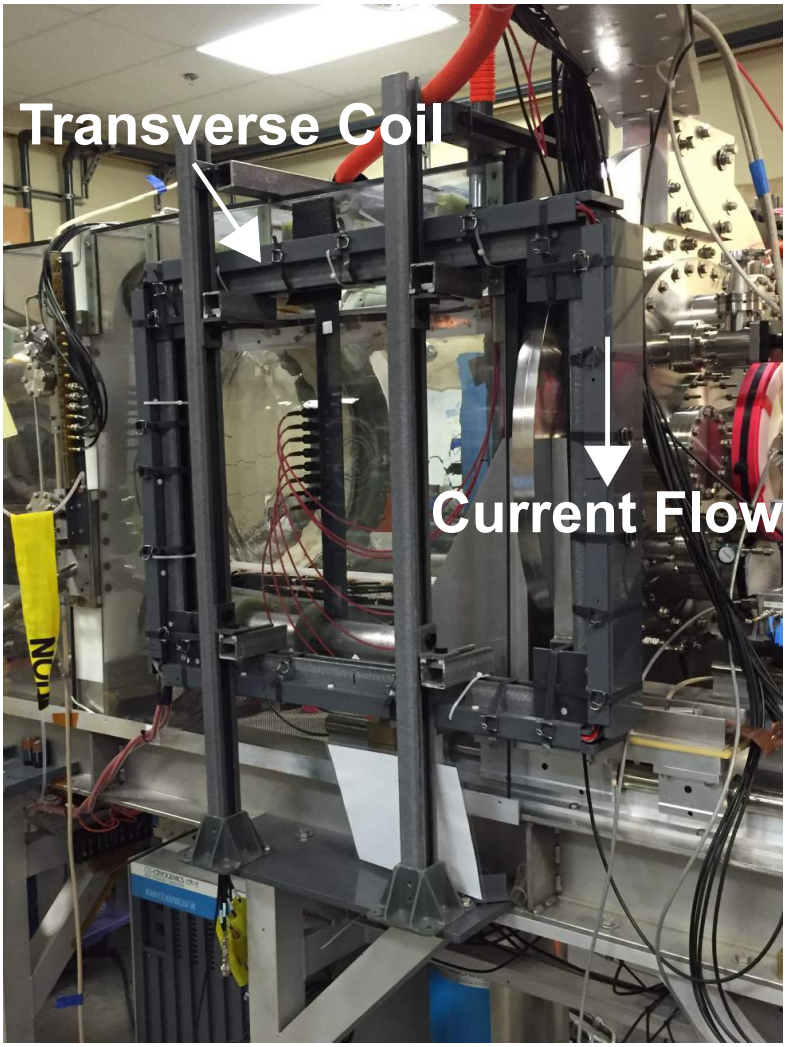

Figure 5.3. Structure of the transverse coil. The shape of that coil is square, and it has another coil on opposite side.

5.3 Diagnostic Suite

Figure 5.4 shows the schematic of arrangement of diagnostics on the test stand. To characterize the ejected CTs the following diagnostics had been set up on the drift tube: magnetic probe, collimated fibers, dispersion interferometer, and triple Langmuir probe. In addition, to measure the trajectory and movement of CT, we usually use the magnetic probe and collimated fiber arrays. However, this

diagnostic system cannot monitor CT's position clearly due to limited views. Thus we have adopted the fast-framing camera. The fast camera can be adjustable the viewing angle by changing the lens, which is mounted on the fast camera.

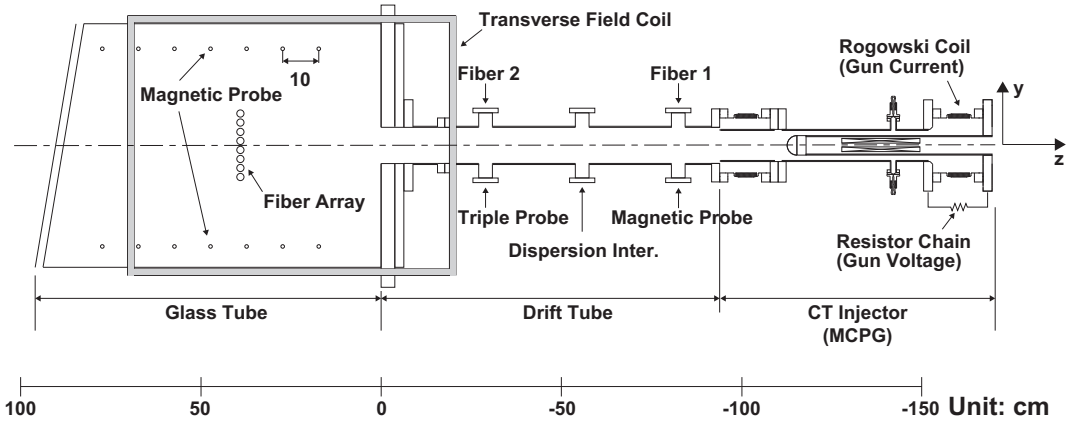

Figure 5.4. Schematic of the diagnostics on the test stand.

5.3.1 Gun current and Voltage Measurement

To measure the gun current and voltage, we used a Rogowski coil on the ceramic break between electrodes and resistor chain connected between electrodes. The Rogowski coil on the ceramic break can measure the gun current through the inner electrode. The voltage is obtained by measuring the current through a 4.5 kΩ resister chain across the gun's breech. Figure 5.5 shows the typical waveforms of gun current and voltage.The maximum gun current is ∼200 kA at the peak. The typical rise-time is approximately 10 μs as shown in Fig. 5.5.

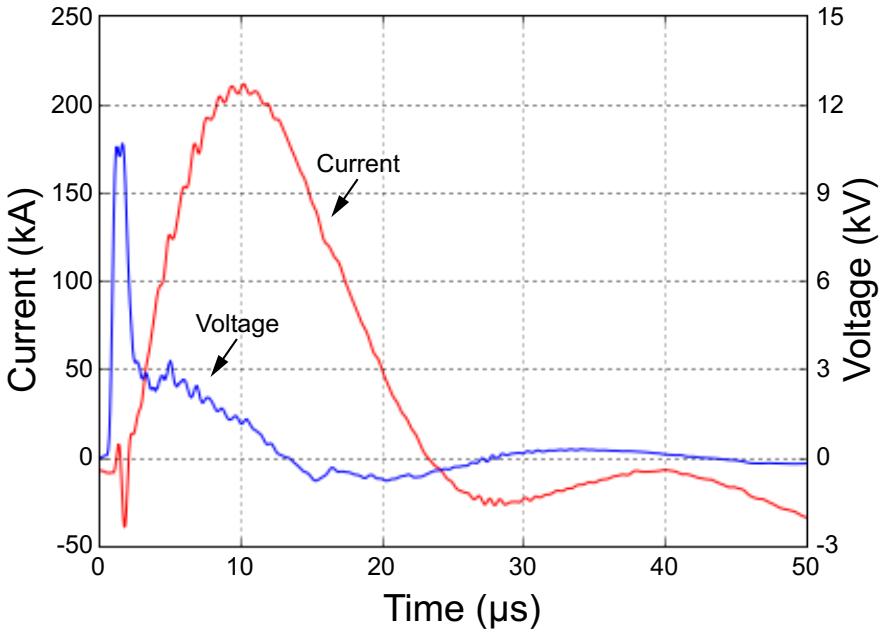

Figure 5.5. Typical waveforms of the gun current (red line) and voltage (blue line). Maximum current at 10 kV of charging voltage is ∼200 kA at around peak.

5.3.2 Drift Tube (velocity, density, and temperature)

The drift tube is made of stainless steel (SS316) with 3 mm thickness. While the CT travels in the drift tube, the chamber wall acts as a flux conserver. In the drift tube, we can measure the typical plasma parameters such as velocity, density, and temperature. Figure 5.4 illustrated the positions of each of diagnostics. The diagnostics on the drift tube are as follows:

- Magnetic probe: Installed on the first port from the MCPG side. The purpose of the magnetic probe is to estimate the trapped flux in the CT as well as to assess the CT's timing and length by picking up the magnetic field.

- Two PMTs with collimated fibers: The PMTs used 1P21, which is sold by Hamamatsu Corporation. These fibers are not mounted line filters. The

first fiber and the second fiber installed on first port and third port, respectively. These fibers can measure the CT's average velocity using time-of-flight method.

- Dispersion interferometer: dispersion interferometer mounted on the second port. It can measure the line-integrated electron density.

- Triple Langmuir probe: Installed on the third port. It can measure a local electron density, and a local electron temperature.

5.3.3 Glass Tube

In the glass tube region, the trajectory of the CT is measured by some diagnostics: magnetic probe, collimated fiber, and fast-framing camera. The glass tube region has a transverse magnetic field, which is comparable to the C-2U confinement axial magnetic field. The magnetic field extends along the machine axis for ∼70 cm from the entrance of the glass tube. Separatrix position of C-2U FRC is situated at about 40 cm from the confinement-vessel wall. The virtual FRC separatrix position on our test stand is around the middle of the transverse coil.

The schematic end-view of the diagnostics setup on the glass tube is illustrated in Fig. 5.6. The collimated fibers aligned along y-axis at intervals of 2.5 cm and can move along the machine axis ranged from 39 cm to 62 cm on the glass tube. Therefore, this fiber array can measure upward and downward motion of the plasmoid the transverse magnetic field which is caused due to the interaction between external magnetic field and the current of CT interactions. The CT pushes

aside the magnetic flux when it penetrates into it. So the magnetic probe array is installed outside surface of the glass tube at intervals of 10 cm along the machine axis as shown in Fig. 5.4, to measure the fluctuation of magnetic field while the CT penetrates.

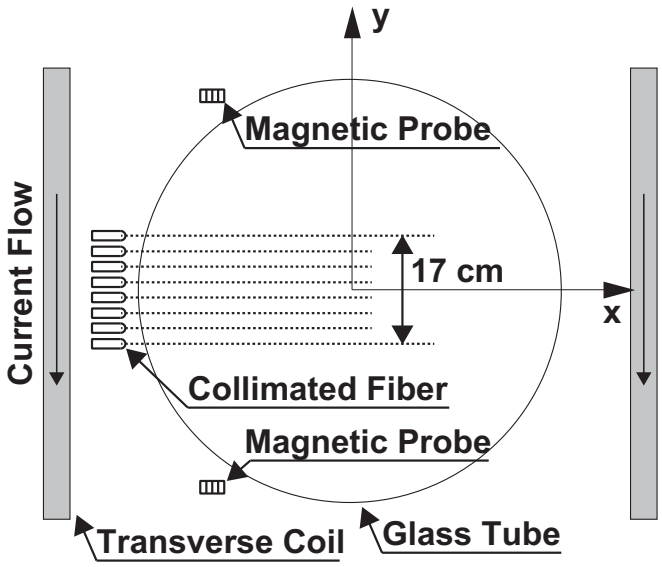

Figure 5.6. Schematic end-view of diagnostics setup on the glass tube.

5.4 Typical Waveforms on the Drift Tube

Figure 5.7 shows the time evolutions of typical waveforms on the MCPG and drift tube: (a) gun current and voltage between electrodes, (b) magnetic field on the drift tube, (c) and (d) signals from PMTs. In case of Fig. 5.7, the centroid of the CT is around the peak of the magnetic probe signal. The CT was ejected at around 15 μs as shown in Fig. 5.7(c). The length of the CT can be estimated from the CT's velocity and the magnetic probe's pulse width. Typical CT parameters are listed in table 5.1.

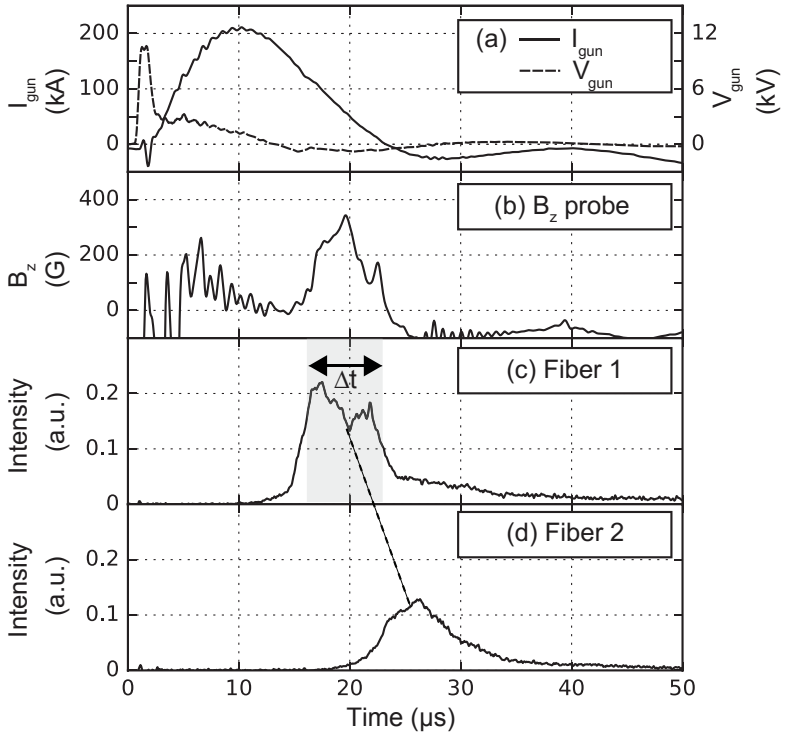

Figure 5.7. Time evolutions of the typical waveforms on the MCPG and drift tube: (a) gun current and voltage; (b) magnetic field at the wall inside vacuum on the first port; (c) and (d) the first and the second PMT signals, respectively. The distance of the Fiber 1 and 2 is 51.4 cm. Filled region indicates the signal due to CT in (c).

Table 5.1: Typical CT parameters on the drift tube.

CT parameters	
Average velocity (km/s)	$\sim$100
Average electron density (cm^{-3})	$\sim 1.9\times10^{15}$
Electron temperature (eV)	$20-40$
Length of CT (cm)	$\sim$50
Mass of CT (μg)	$\sim$12

5.5 CT Energy

Figure 5.8 shows the energy density estimated from the electron density and velocity. Since required energy is 4 kJ/m^3 for the C-2U external field, the energy density must be higher than 4 kJ/m^3. To estimate the energy, we have used the dispersion interferometry for the electron density measurement and collimated fibers to

estimate the average velocity. Usually, the ejection velocity can be controlled by changing the stored energy, the bias magnetic field, and the amount of gas. Figure 5.8 changed only amount of gas. Other parameters such as stored energy is fixed. In case of slower velocity, gas volume is higher than faster speed case. To control the gas volume on our device, the gas puff system can control the gas duration and back ground gas pressure. The achieved kinetic energy density satisfies the requirement. Therefore, the CT can penetrate the transverse magnetic field to fuel the FRC.

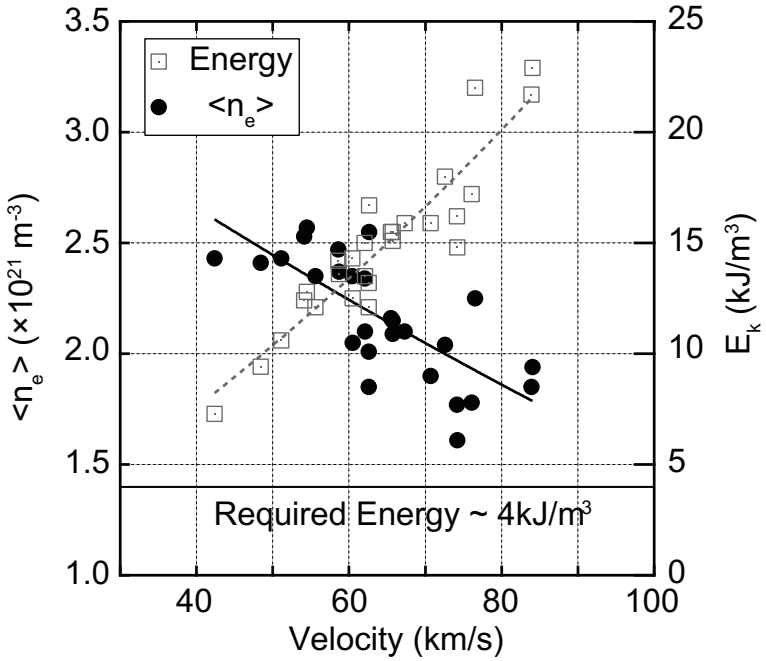

Figure 5.8. Correlation between electron density and velocity in the drift tube. $< n_e >$ and E_k are average electron density and kinetic energy from density and velocity, respectively. Required energy to penetrate is 4 kJ/m^3.

5.6 CT Penetration into Transverse Magnetic Field

In order to evaluate the behavior of an injected CT inside the transverse field, the CT injection into the transverse field was demonstrated with the tokamak's

external field at JFT-2M with high magnetic field, i.e., greater than 1.0 T [28]. It was confirmed that the CT shifted by Lorentz force between poloidal current of the CT and the external field. On the other hand, the magnetic field of the FRC is smaller than tokamak. Therefore, we should evaluate the trajectory of the CT inside magnetic field. In this section, we describe the CT's trajectory inside the external field such as FRC device.

A CT passes through the drift tube and then penetrates a transverse magnetic field. Figure 5.9 shows time evolution of magnetic signals obtained from the upper and the lower arrays. The schematic end-view of the diagnostic setup on the glass tube is illustrated in Fig. 5.6. Both magnetic probe arrays are arranged at positions away from the axis of the coil; therefore, the measured magnetic field at the probe position is weaker than on-axis. Left figure shows vacuum field at probe position before CT penetration from each position; the red line shows upper side, blue line shows bottom side, as shown in Fig. 5.6. The typical position of separatrix r_s of C-2U FRC is depicted in Fig. 5.9 to indicate the CT penetration; the line indicates the distance from the vessel wall to separatrix radius. When a CT penetrates the transverse magnetic field, the injected CT excludes the magnetic flux and the magnetic probe signal decreases because the direction of the magnetic field change by excluding the transverse magnetic field. Also, the glass chamber is not a flux conserver. Right figure on Fig. 5.6 shows fluctuation of the each magnetic probes. The first magnetic probe at $z = 21.1$ cm was detected the fluctuation at $t = 34$ μs. The CT's velocity can be estimated by time-of-flight method from the magnetic probe measurement. The estimated

axial velocity reaches 100 km/s at the initial time as indicated by solid lines in the figure. This speed is consistent with the one obtained on the drift tube and and it reach at the $z = 41.1$ cm, which is position of the separatrix radius.

Figure 5.10 shows a relationship between magnetic probe and PMT signals. As shown in Fig. 5.7(d), the CT starts to travel into the glass tube region around $t = 30$ μs. In the case shown in Fig. 5.7, the CT penetrates the field at $t = 32$ μs, and then the probe signals on $z = 20 - 30$ cm decrease. The collimated fiber array also shows an enhanced emission around $z = 42$, 60 cm at $t = 30$ and 32 μs shown as contours in Fig. 5.10. At these times, the magnetic signals at 40–60 cm do not decrease. We can assume that this emission is from initial plasma, which was generated by the initial high-voltage breakdown between electrodes. Due to an injected plasma, the transverse magnetic field is frozen and the magnetic field increases locally. Thus the magnetic field increases at emission time before CT penetration. After CT penetration, the probe signal decreases until $t = 34$ μs, and the upper magnetic probe signal changed from negative to positive ($t = 38$ μs). On the other hand, if the CT is injected into the glass tube without the transverse magnetic field, it expands with Alfven time so that it is not compressed by magnetic field. Therefore, the magnetic probes will measure the CT's magnetic field density. In fact, the magnetic probes measured a fluctuated magnetic flux.

To measure the trajectory and movement of the CT, we usually use the magnetic probe and collimated fiber arrays. However, these diagnostics cannot monitor position clearly due to limited views, i.e., local measurement at each probe/fiber position. Thus we needed a qualitatively different diagnostic to observe global

motion. Accordingly, we adopted the fast-framing camera for trajectory measurement of CT in the magnetic field. Figure 5.11 shows a time sequence of contour map of emission of light inside the glass tube taken by the fast-framing camera. Frame rate and exposure time in this shot are 600 kHz and 1.5 μs, respectively. When the CT's velocity is 100 km/s, displacement of the CT during exposure is 15 cm. The camera is mounted to see a side-view of the glass tube. The CT enters from right-hand side of picture and moves to the left. The fiber array is casted on the left side on each figure. The camera image shows similar behavior as the fiber signal shown in Fig. 5.10 (t = 30 and 32 μs). Following the initial plasma, the CT (core plasma) penetrates the transverse magnetic field at t = 36 μs and moves downward.

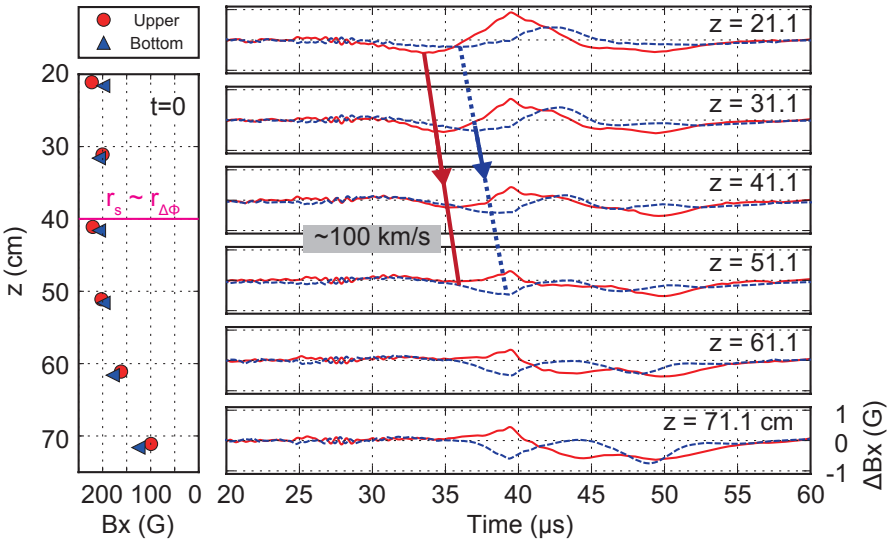

Figure 5.9. Time evolution of magnetic probe signals obtained by the upper array (red line) and the lower array (dashed blue line). Left figure shows vacuum field at probe position before CT injection; the dashed lines connecting initial peaks of waveforms. A separatrix position of FRC corresponds 40 cm from entrance of the glass tube.

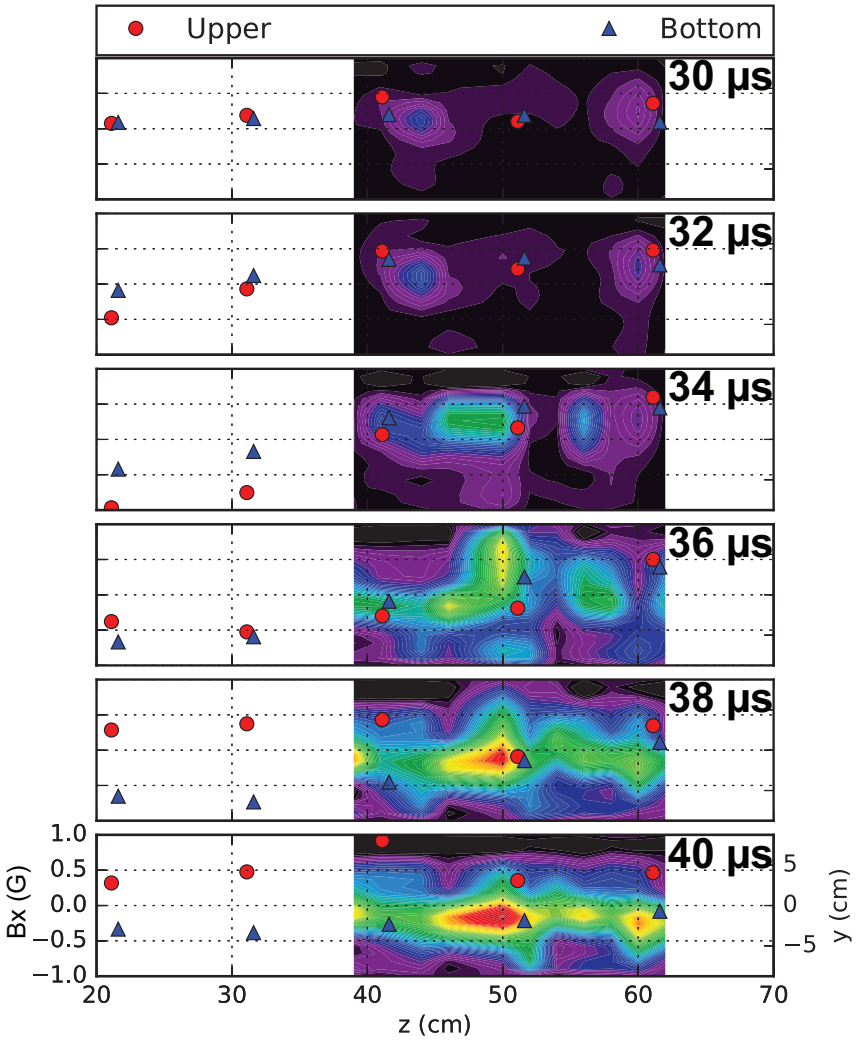

Figure 5.10. Relationship between axial magnetic probe array (markers) and radial collimated fiber array (contour plot). Penetration of CT starts around 30 μs. Area scanned by fibers is from 39 cm to 62 cm in z direction and $\pm$8.5 cm in y direction.

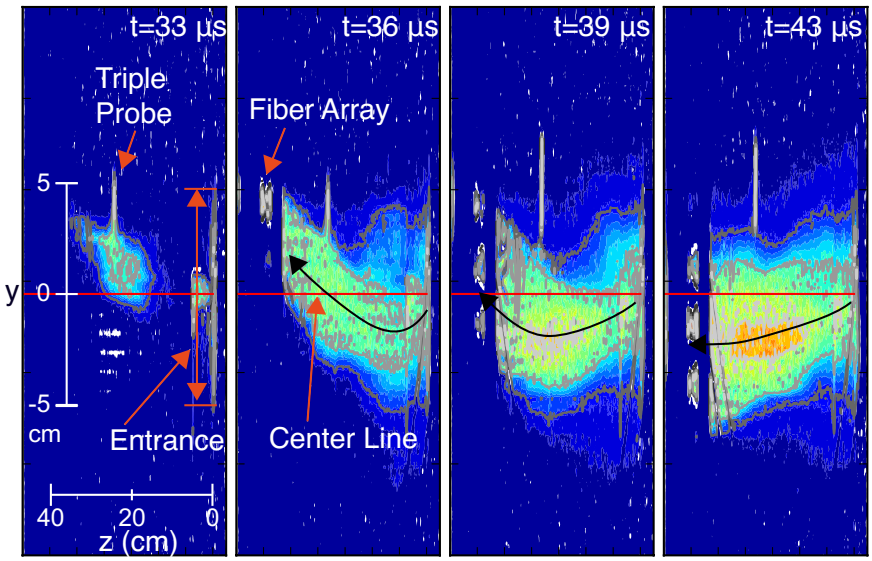

Figure 5.11. Time evolution of light emission taken by the side-view fast-framing camera. Shutter speed and exposure time are 600 kHz and 1.5 μs, respectively. Black line shows the CT's trajectory.

5.7 Multi-pulse CT ejection/penetration

The multi-pulse CT injection system constructed on the test stand and tested. This system can operate with 2 CTs, as shown in Fig. 4.6. The gas puff does not necessary for second CT because the neutral gas is already distributed inside the vacuum region which is puffed for the first CT penetration.

Figure 5.12 shows a comparison of the line-integrated electron density between first and second CTs. $T = 0$ is a trigger time of the main discharge. The gas puff turn off a power supply at $t = 0$. To compare the electron density, the duration of the gas puff valve varied, and other conditions such as gas pressure and bias magnetic field were fixed. The first CT's density decreased about 30%. On the other hand, the density of second CT did not change. As a reason of this result,

the neutral gas spread along the machine axis by thermal diffusion. Thus the CT ionizes a neutral gas and scrambles up plasmas. Then CT's density increases.

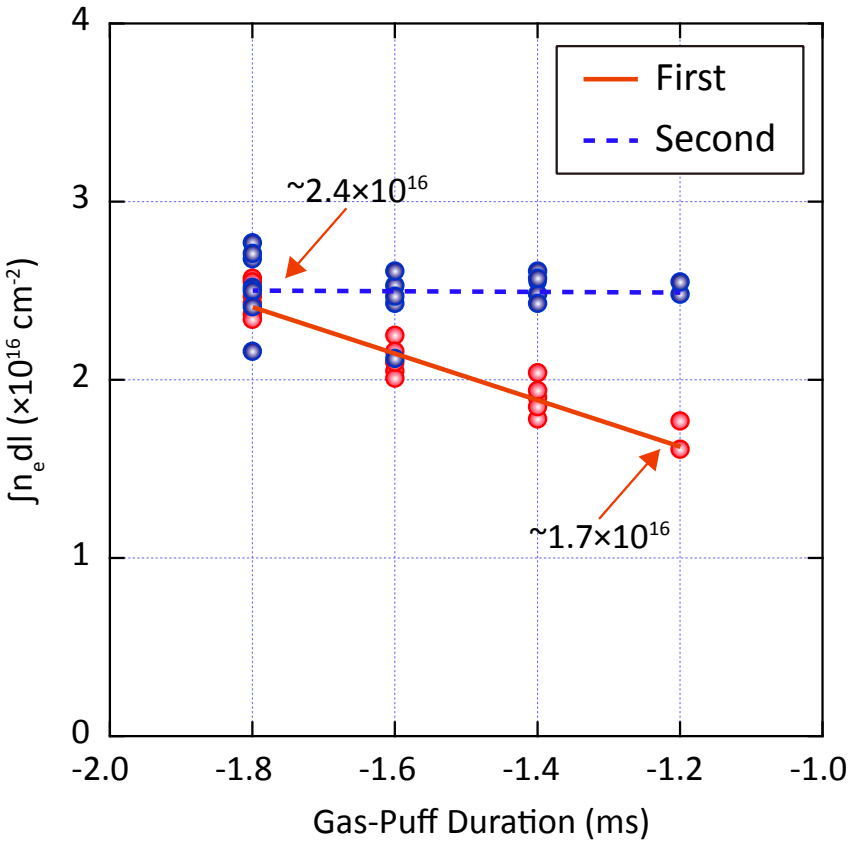

Figure 5.12. Comparison of line-integrated electron density between first and second CT. $T = 0$ is trigger time of the main discharge. The first CT can control density by varying gas puff duration. On the other hand, the density of second CT does not show the relation.

Chapter 6

Compact Toroid Injection into FRC

6.1 Setup for the CT Injection on the C-2U

6.1.1 Installation of the CT injectors

Figure 6.1 shows the installation of the location of the CT injectors on the C-2U confinement vessel which has an inner diameter of 1.4 m. Figures 6.1(a) and 6.1(b) shows the top and axial views from the south side, respectively. The CT injectors were mounted on the NC and SC plane. The north CT injector was mounted on the 45 degrees port at the NC plane. On the opposite side, another CT injector was mounted on the 225 degrees port at the SC-plane. Also, both CT injector is oriented at the angle with respect to the z-axis and both CT injector installed on C-2U 180 degrees apart as shown in Fig. 6.1(a), and vertical angled such that the injected CT's trajectories intersect at the center of the confinement vessel as shown in Fig. 6.1(b). The angles of each CTIs are; North CT is -26.1 degrees from A-plane and -42 degrees from vertical. South CTI is 29 degrees from A-plane and

-39.3 degrees from vertical. Also, both CTI has a distance of 1 m.

The south CT injector which mounted on the lower side has a multi-pulse system that can inject two CTs with a repetition rate up to 1 kHz. Therefore, we can inject the 3 CTs in the configuration lifetime of the C-2U FRC: One CT by the North injector and 2 CTs by the South injector.

To assess the CT trajectory inside the confinement vessel, we mounted the fast-framing camera onto the confinement vessel. Figure 6.2 shows the location of the fast-framing camera. The camera was mounted on the NJ port and slightly looks up from the downside. The viewing angle was covered overall from middle of a vessel to formation section. Therefore, the both CT's trajectory is covered and able to see by a camera. Also, the FRC's motion also can take a picture/movie.

In this section, we mention diagnostics system to assess the injection on the C-2U confinement vessel, and results describe what had happened by CT injection.

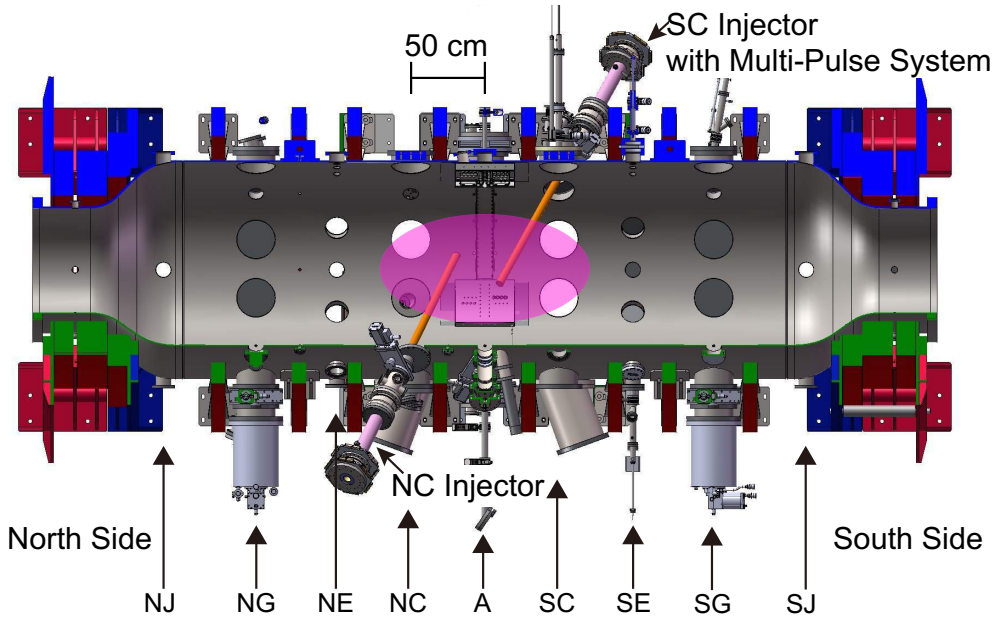

(a)

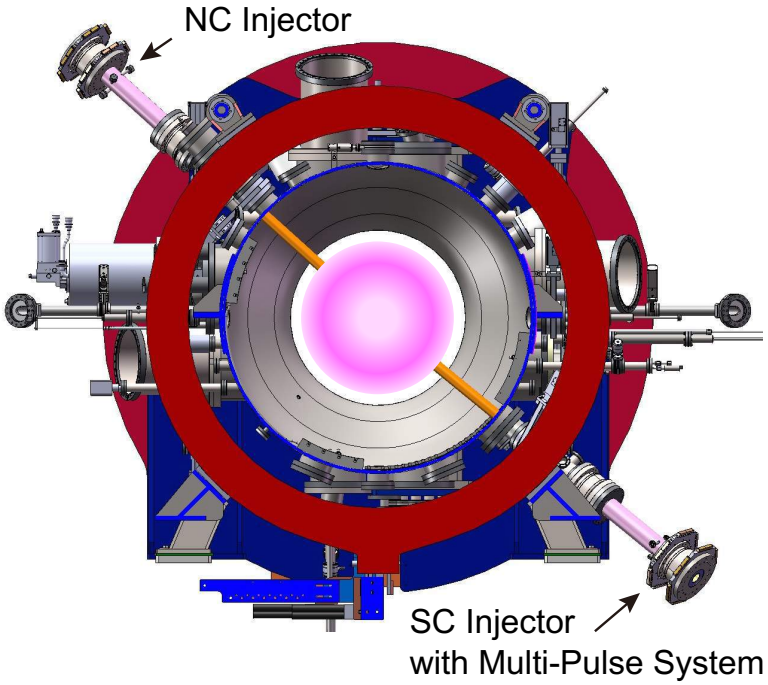

(b)

Figure 6.1. Installation position of the CT injector on the C-2U vessel. (a) Top-view and (b) Axial-view from south.

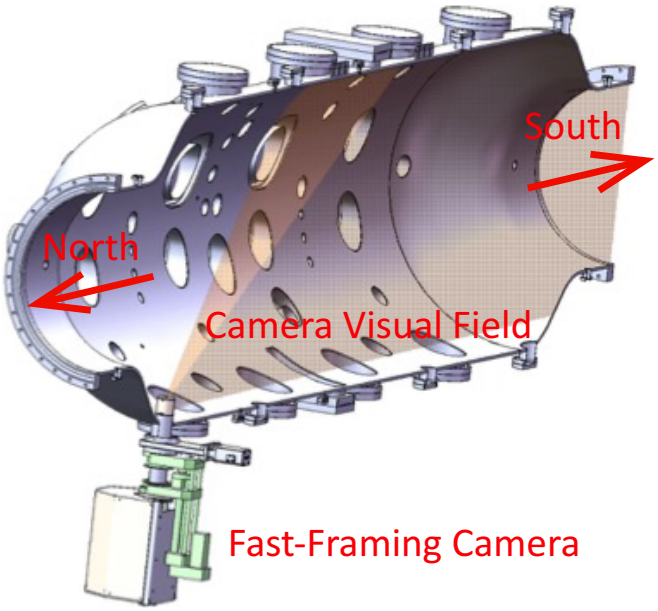

Figure 6.2. The location of the fast-framing camera. The camera was mounted on the NJ port and slightly looks up from the down side.

6.1.2 Diagnostic suits

On the C-2U device, many diagnostics install on the confinement vessel [46], that includes magnetic sensors [36, 45], interferometry [15], spectroscopy [16], bolometory [46], fast ion measurement [13, 23]. The role of the main diagnostics to investigate a behavior of global FRC motion are as follows;

1. **Magnetic probe**

   The magnetic probe are used as a magnetic sensor and installed inside the confinement vessel in order to metal chamber. The geometries of the FRC such as excluded-flux radius $r_{\Delta\phi}$, length l_s, and volume V are measured by magnetic probes. The separatrix length l_s is defined as the half-width of the axial profile of excluded-flux radius. The volume V of an FRC estimate from the distribution of the excluded-flux radius along the z-axis. Then, the

volume can define as $V = \int \pi r_{\Delta\phi}^2 dz$.

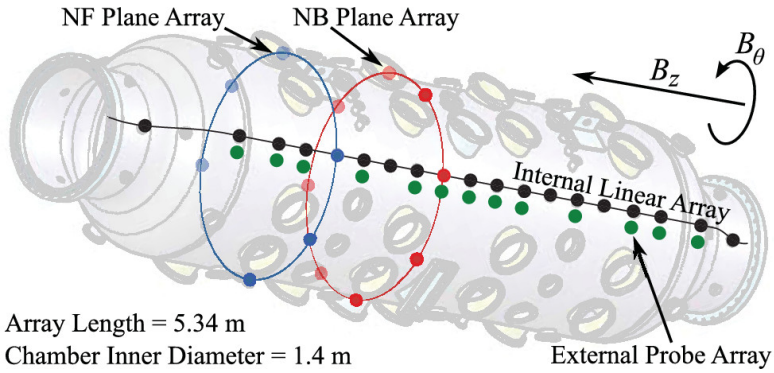

Figure 6.3. Schematic showing the location of magnetic probes in the linear and azimuthal arrays on the confinement vessel (adopted from [45]).

2. CO_2 interferometer

To measure the electron density inside the confinement vessel, the CO_2 interferometry is used. Figure 6.4 shows the interferometry system at the mid-plane. The impact parameters of the probe beams are -3.3, -15, -20, -25, -30, and -35 cm. When a probe laser beam is propagating inside the plasma, the phase change due to plasma is directly related to plasma electron density. So the phase shift by electron is defined as;

$$\phi_p = 2.82 \times 10^{-15} \lambda \int n_e dl \tag{6.1}$$

where λ is the laser wavelength in vacuum, and integration is showing the line-integrated electron density. The wavelength of CO_2 laser is 10.6 μm.

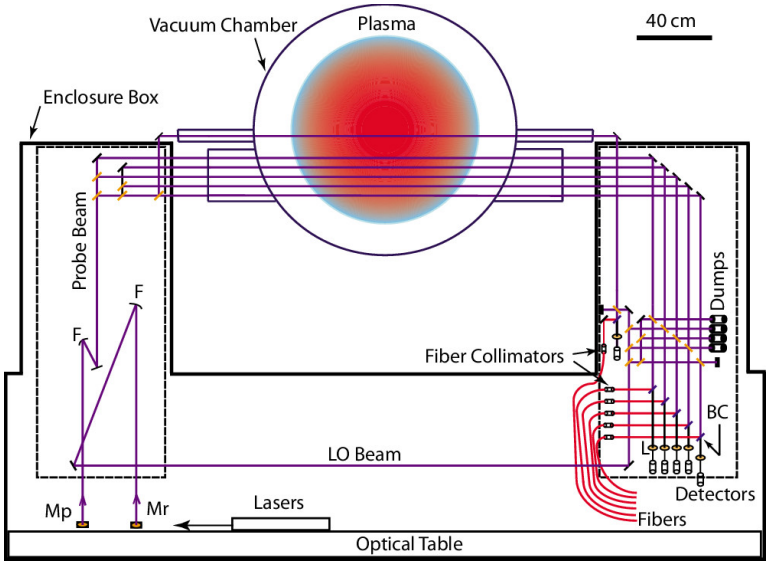

Figure 6.4. Enclosure box and opical layout on vertical breadboard: (F) focusing mirror, (BC) beam combiner, and (L) lenses (adopted from [15]).

3. **Spectroscopy**

Figure 6.5 shows schematic and viewing chords for the viewports C and E.

- Ion Doppler Spectroscopy

  To simultaneously measure the ion temperature at different radial and axial locations, a multi-chord ion-Doppler diagnostics is developed. The viewport on the C-2 device are located at C-port, which is symmetric to the machine center. The ion Doppler spectroscopy system is applied to observe the temperature of impurities ions in FRC. For high temperature FRC plasma, an Oxygen-V emission line is typically selected.

- D-alpha Emission

  The eight channels D-alpha monitors are developed to measure the absolute intensity of the Deutrium-alpha line, which is Balmer-α line emis-

sion. For the light signal with spectral radiance $S(\lambda, t)$ collected by the collimator of area A_c and the solid angle Ω of a D-alpha channel, which uses a filter with normalized response function $F(\lambda)$, the PMT signal current $I(t)$ is give by

$$I(t) = \mathrm{K}\Omega A_c \int F(\lambda)\, S(\lambda, t)\, d\lambda \tag{6.2}$$

where K is a proportionality constant that accounts for detector gain, response.

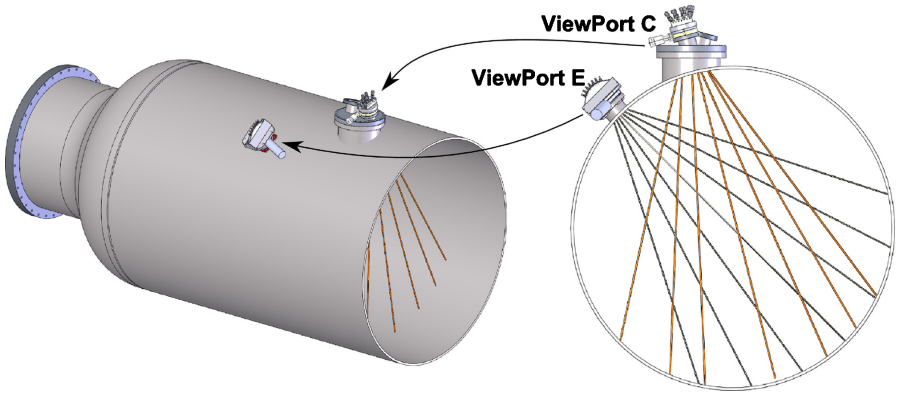

Figure 6.5. Schematic and viewing chords for the viewports C and E. Left illustration shows the locations of these view ports on the symmetric-half of the confinement vessel. Right illustration shows the line of sight of the each collimators (adopted from [16]).

4. **Bolometry**

On the C-2U confinement vessel, bolometers are installed to measure the total particle flux and neutral particle energy emitted by FRC and the confinement vessel wall. The bolometers are mounted in fan-array; thus, signals can indicate the FRC's global motion/instabilities, such as wobble ($n = 1$) motion.

5. **Fast Ion Measurement**

   The fast ion which is generated from the NBI distributes around the FRC. This particles works for well confinement the FRC, i.e., the pressure of the FRC is balanced between FRC's pressure, external magnetic field, and fast ion's pressure. For the measurement of the fast ion, the neutral particle analyzers (NPA) are employed. The escaping fast hydrogen atoms are detected by an NPA. A neutral beam can provide a local source of atoms in the core plasma with which fast-ions can charge-exchange. In addition, the secondary electron emission detector is used in order to measure the shine-through of the NBI [14].

6.1.3 Estimation of penetration depth of CT into vacuum

As mentioned in CTI test stand section, the CT must cross the external field, which is surrounding the FRC. Therefore we simulated by constructing the transverse magnetic field on the test stand. As a result, the CT could pass through the transverse magnetic field. The next step we tested a penetration into the vacuum confinement vessel on the C-2U confinement vessel. This section shows the result of CT injection into a vacuum vessel.

Figure 6.6 shows a composite image which of CTI only and FRC only. The CT was penetrated from lower port, as shown in Fig. 6.6. A dashed line shows the excluded-flux radius. At this time, FRC's radius was 33 cm. From this estimated value, the diameter of CT at this time was $8.0 - 9.0$ cm. This means that the penetrated CT did not compress by magnetic field. Also the penetrated CT

reached separatrix easily, i.e. the CT can easily collide with FRC.

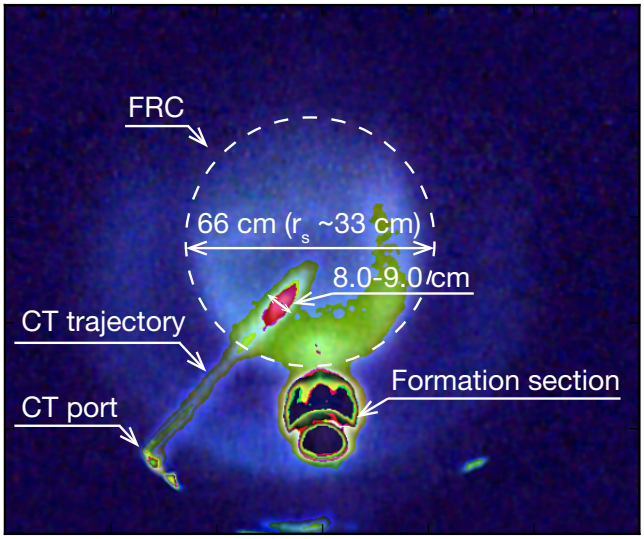

Figure 6.6. Composite image which of CTI only and FRC only.

6.1.4 Measurement of CT's density by CO_2 interferometer

The trajectory of the injected CT passes to the vicinity of the CO_2 interferometer chords. Thus the interferometer will be measured the density of the moving CT. Figure 6.7 shows time evolution of the line-integrated electron density measured by CO_2 interferometer. The CT come from south CT injector then the signal is started from the outer chord. Therefore the CT did not travel across the chords between -30 to -35 cm. On the other hand, the CT passed through the innermost chord at $y = -3.3$ cm while it is keeping the high density ($\sim 3 \times 10^{15}$ cm^{-2} at $y = -3.3$ cm).

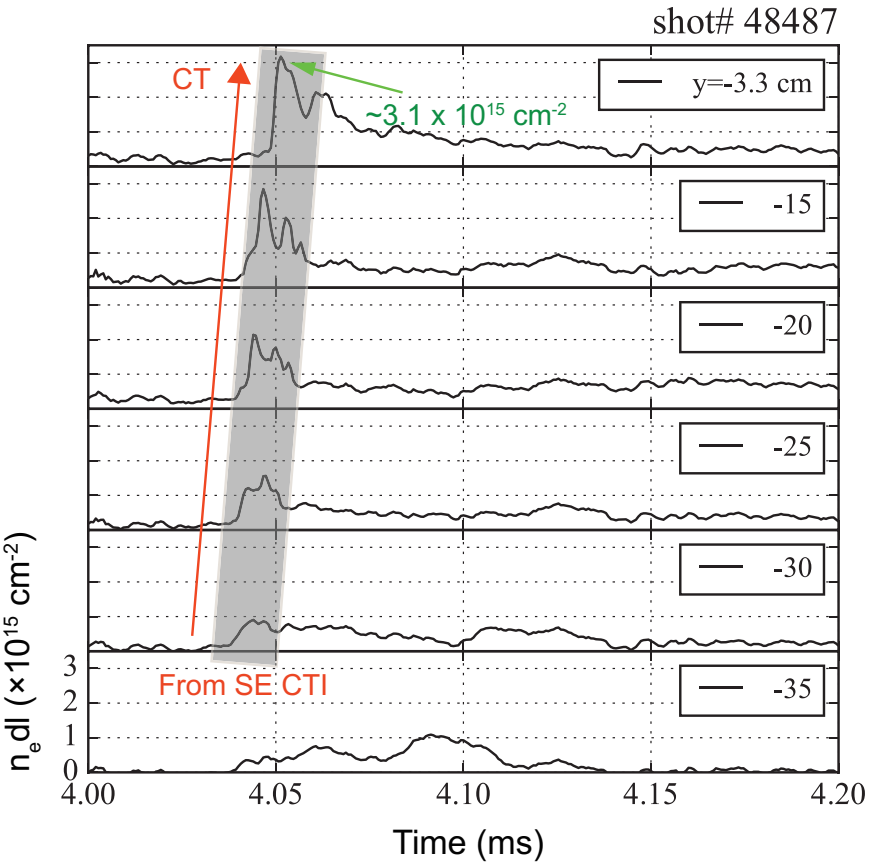

Figure 6.7. Time evolution of line integrated electron density by CO_2 interferometer. The CT injector was triggered at 4 ms in this shot and the CT is penetrated into the confinement vessel without the FRC.

6.2 Results of CT Injection into C-2U FRC

6.2.1 Optimization of CT injection time

As shown in the introduction section, the recent FRCs are sustained by NB system, and the lifetime is dramatically extended. However, the particle inventory decreases by spontaneous particle loss. Also, the energies of the FRC such as thermal energy and magnetic pressure is also decayed. Therefore, the CT injection needs an estimation of the injection time to keep power balance. To estimate

the CT injection time, the CTs injected in an interval with 0.5 ms from one side. Figure 6.8 shows a comparison of effect of the CT injection time. As a result, the rate of increase of particle number tended to be low in late time. Thus, the timing before 2.0 ms satisfies minimum requirement on C-2U.

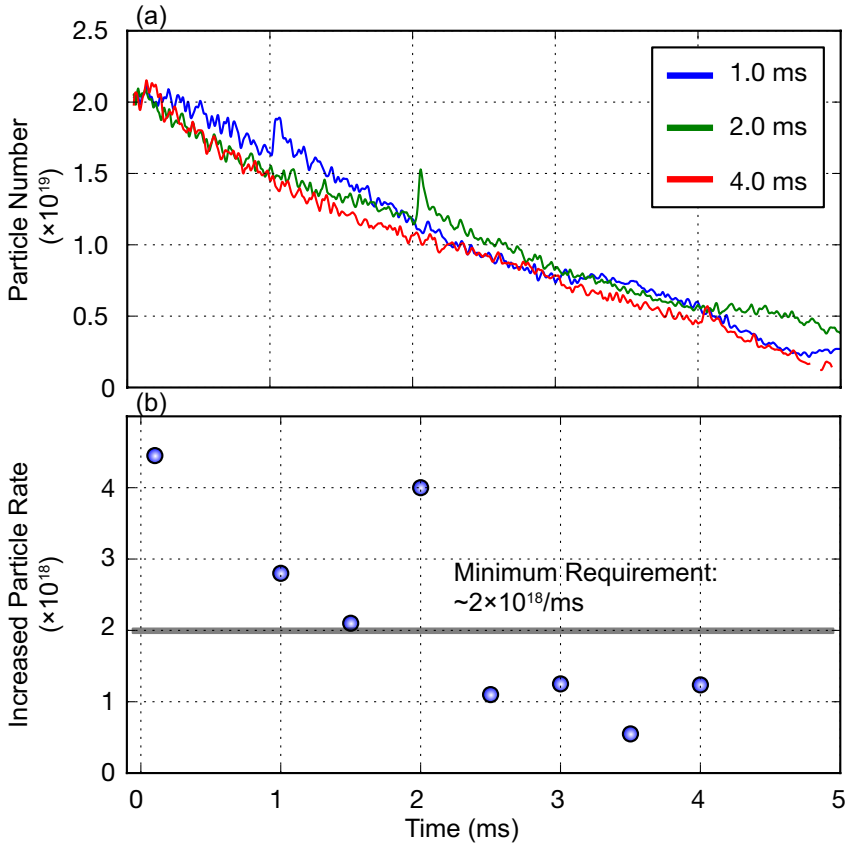

Figure 6.8. Comparison of effect of the CT injection time. (a)time evolution of the particle number for each CT injection time. (b)Increased particle rate of each CT injection.

6.2.2 Change in Geometry of FRC by CT Injection

Figure 6.9 shows the time evolution of the FRC geometry: separatrix radius, a length of the FRC, and volume of the FRC. The CT injected at 1.0 ms and 3.5 ms in this shot. At 1.0 ms two CTs are injected at the same time from both side, and single CT injected from south side at 3.5 ms. The separatrix radius is shriven

by the CT injection. However, disruptive reduction of the separatrix radius is not shown in this shot. The length of FRC also shrunk at the same time with separatrix radius. According to these result, the volume of FRC reduced by the CT injection.

Due to decrease the poloidal flux, a resistivity inside the FRC will increase by increasing in particle inventory [12, 20]. The magnitude of the poloidal flux can be determined from maxwell's equations. The changing rate of poloidal flux is defined as

$$\frac{d\phi_p}{dt} = -2\pi(rE_\theta)_{r=R} \tag{6.3}$$

where the Faraday's law applied the integral form over the area, and E_θ is an azimuthal electric field. This equation means that the poloidal flux loss occurs at magnetic axis, $r = R$. Using a simple Ohm's law, the relation between resistivity and field is produced

$$\frac{d\phi_p}{dt} = -2\pi R\left(\frac{\eta}{\mu}\frac{dB_z}{dr}\right)_{r=R} \tag{6.4}$$

From this equation, it proved relationship of poloidal flux loss rate at field null point which is magnetic axis on the FRC. In addition, the field gradient dB/dt can be written as

$$\frac{dB_z}{dt} = B_z\left(-\frac{1}{2}\frac{d^2\beta}{dr^2}\right)^{1/2} \tag{6.5}$$

where, β is average beta. Also, the resistivity is defined as Spitzer resistivity η^{sp}.

$$\eta^{sp} = 0.51\frac{m_e^{1/2}e^{1/2}\ln\Lambda}{3\varepsilon_0^2(2\pi T_e)^{3/2}} \tag{6.6}$$

$$= 1.65\times10^{-9}\frac{\ln\Lambda}{T_e(\mathrm{keV})^{3/2}} \qquad (\Omega\cdot m) \tag{6.7}$$

where $\ln\Lambda$ is coulomb logarithm. In usual plasma as fusion device, it use $15\sim20$ as a coulomb logarithm. In usual, the resistivity at the null-point compares to the resistivity of the classical model η^{sp}. Actual an inferred resistivity has an anomaly factor, η/η^{sp} is greater than $8-20$ times. Also, as a theory of based on turbalence from low-frequency-drift (LFD) instabilities has been developed for FRC to explain the flux and particle loss in an FRC [24]. A crude estimation of the confinement time of the poloidal flux τ_ϕ from LFD derive;

$$\tau_\phi \simeq \frac{3\times10^{-8}Br_s^2}{T_e\left(1+{}^{T_e}\!/_{T_i}\right)^{1/2}} \tag{6.8}$$

From eq. 6.7 and 6.8, the decaying rate of the poloidal flux is defined by cooling the electron temperature. Due to this relationships, the FRC which was injected CT cooled the electron temperature by increasing the particle inventory, or the CT cooled the FRC due to lower electron temperature. Therefore, the FRC is shrunken.

Figure 6.10 shows poloidal flux decay late. The poloidal flux is decreased with the lapse of time due to CT injection. Figure 6.10(a) shows the time evolution of the poloidal flux, and figure 6.10(b) shows a decrement of poloidal flux $d\phi/dt$

in 1 ms. The CT was injected at 1.0 ms and 3.5 ms. After CT injection, the poloidal flux signal decreased sharply which compared with the decaying rate of the without CT injection case. On the other hand, the decaying rate changed to slower after a few hundred microseconds as shown in Fig. 6.10(b). So, the FRC with CT relaxed and mitigated to usual FRC. From this meaning, the refueled FRC preserved a configuration as an FRC.

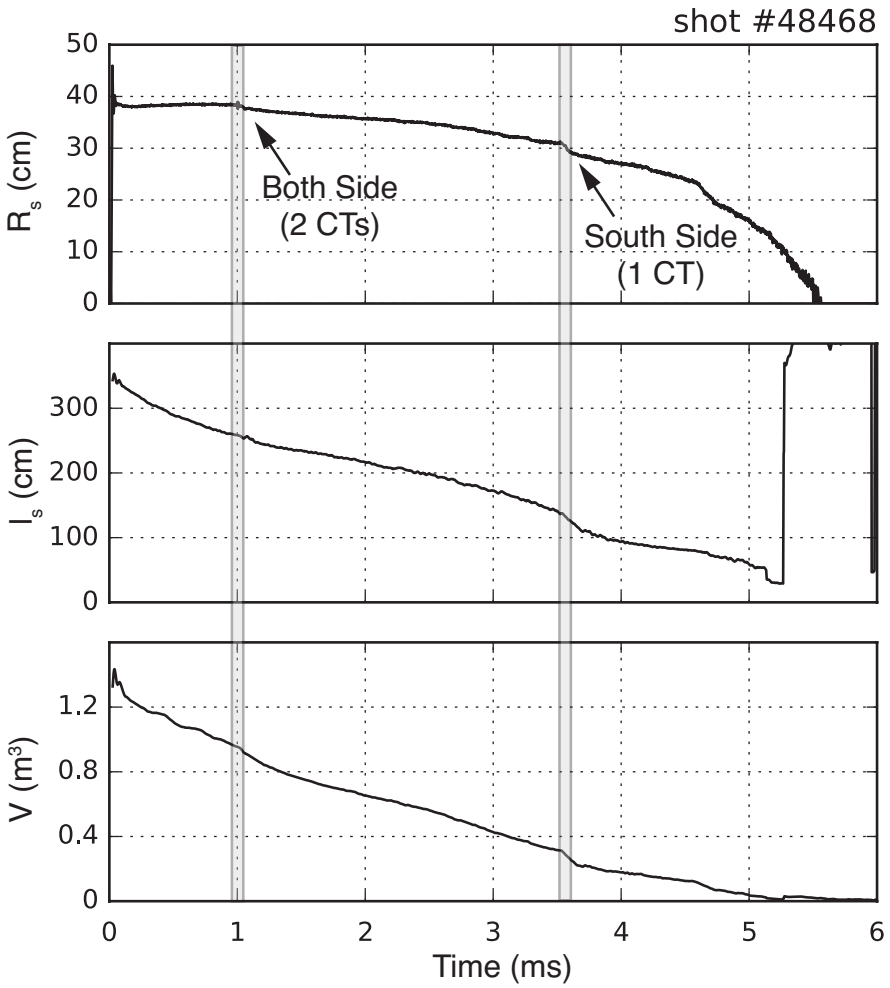

Figure 6.9. Time evolution of FRC geometry: separatrix radius, length, and volume.

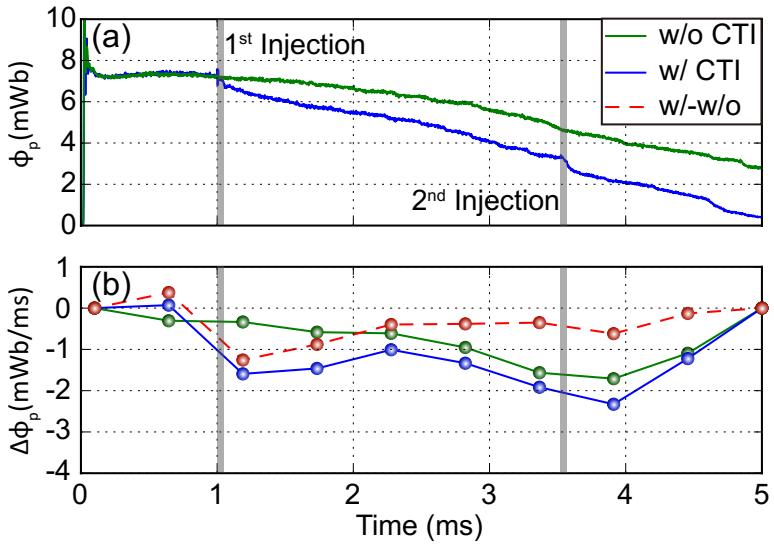

Figure 6.10. Time evolution of: (a) poloidal flux w/ and w/o as function of time, and (b) decay rate of poloidal flux. Green line shows w/o CT, blue line shows w/ CT, and red line shows differential between w/ and w/o CT. The decay rate was changed after CT injection. On the other hand, the decay rate after a few microseconds changed to same decay rate with case of w/o FRC.

6.2.3 Density and Particle Number

Figure 6.11 shows the time evolution of the line-integrated electron density of each chord: y = -3.3, -15, -20, -25, -30 and -35 cm. Figure 6.12 shows a comparison of the line-integrated electron density between the cases with and without CT injection. The red, black, and blue lines indicate: with CT injection, without CT injection, and the difference between with and without CT injection, respectively. Line-density measured by chords around the center (-3.3 and -15 cm) is increased at injection time and maintain higher density. On the other hand, there is no significant change in outer chords. As shown in Fig. 6.9, the FRC shrunk at the CT injection time (t = 1.0 ms and 3.5 ms). The interferometry measures the line-integrated electron density along the path of the laser. Usually, the line-

integrated density decreases when the FRC shrink because a path length of the laser is reduced if the averaged density does not change. However, the density innermost chord increased for long stretch of time. This result suggests the CT enters core region of FRC and then supplies particles into the FRC. The increased rate of density at both injection times is 20% and 14%, respectively.

Figure 6.13(a) shows the time evolution of the particle number, and Figure 6.14 shows a comparison of the particle number with and without CT injection. To estimate the particle number of an FRC, the volume and the averaged electron density is used, i.e., $V \cdot \langle n_e \rangle$, where $\langle n_e \rangle$ is averaged density from line-integrated electron density and diameter of the FRC. The particle number increased 17% ($\sim 4 \times 10^{18}$) due to first CT injection. The rise time of the CT injection was a few hundred microsecond in this shot. Usually, the diffusion time of the CT in vacuum magnetic field is from a few ten microseconds to no longer than 100 μs. Therefore, that time scale suggests that the CT was surely injected into the core region of FRC. The FRC retained the particles injected by the CT for a long stretch of time. On the other hand, the second CT injection at 3.5 ms does not shows significant particle number increase. From these results, the CT should be injected before decreasing phase of the FRC, i.e., the FRC cannot absorb a CT in this period because the confinement magnetic flux of FRC is decreased. Figure 6.13(b) shows the peak flux of the FRC. When the CT is injected, the FRC's flux decreased at both CT injection times. The flux at second CT injection is more than twice as small as the flux at the first CT injection, i.e., the FRC size is considerably smaller than at the first injection. Therefore, the increase of the particle number could

not be seen.

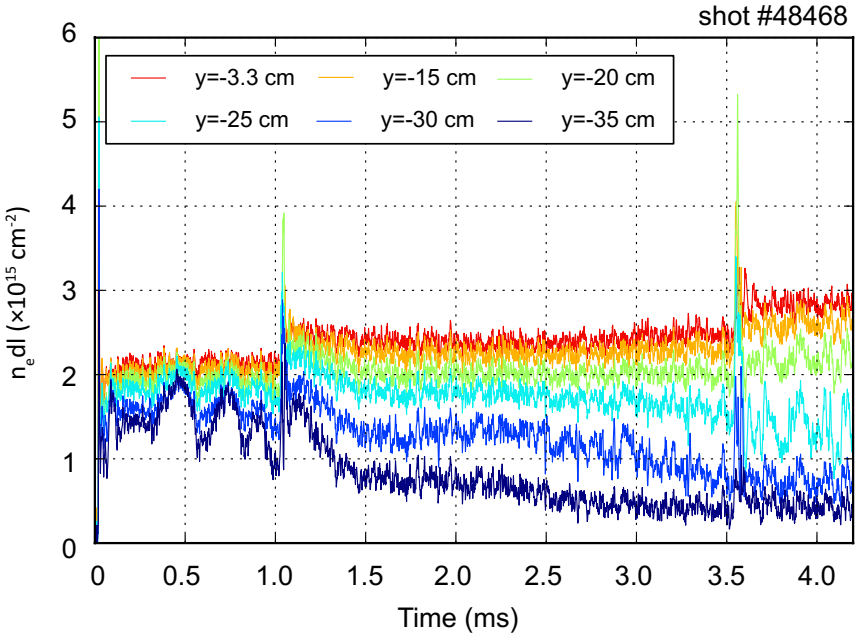

Figure 6.11. Time evolution of the line-integrated electron density of each chord: y = -3.3, -15, -20, -25, -30 and -35 cm. Line-density measured by chords around center (-3.3 and -15 cm) are increased at injection time and maintain the higher density. On the other hand, there is no significant change in the outer chord. after CT injection.

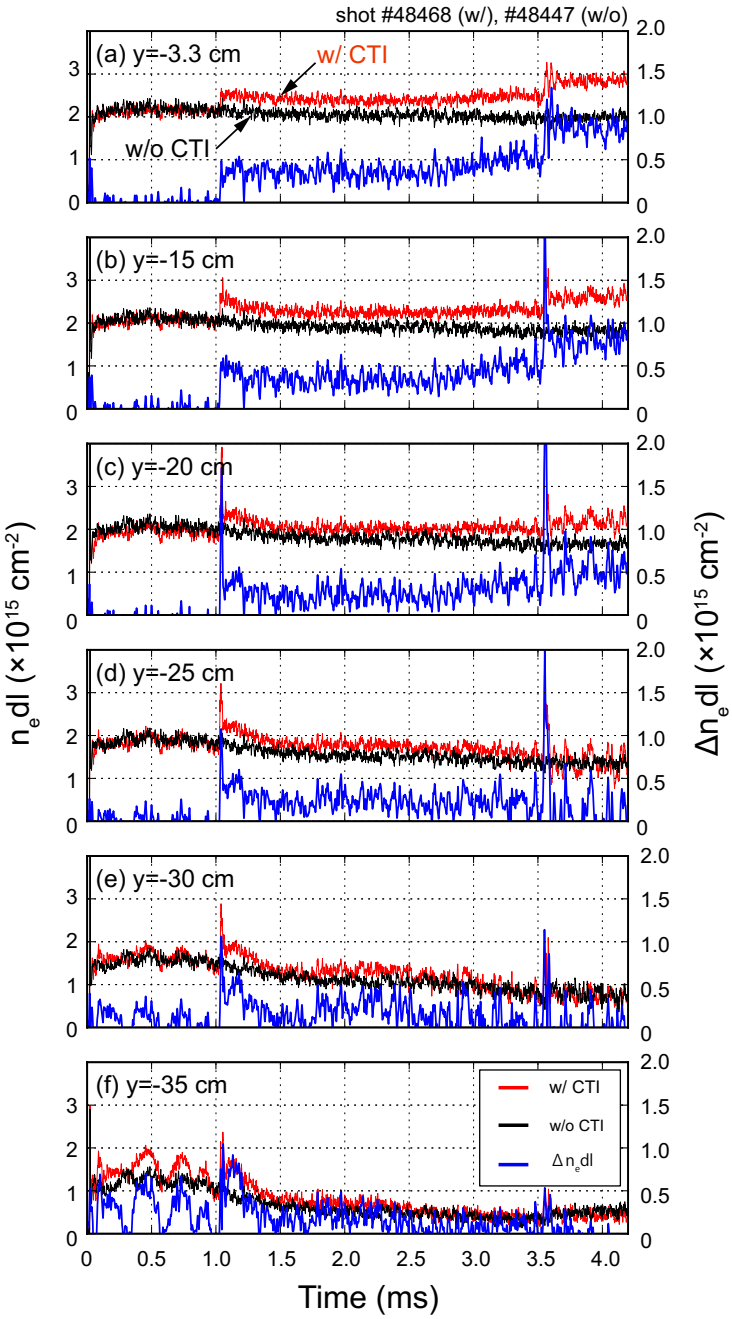

Figure 6.12. Comparison of the line-integrated electron density with and without CT injection. The red and black lines are with and without CTI, blue line indicates difference of the densities. The line-integrated density was increased 20% (0.4×10^{15} cm^{-2}) at 1.0 ms by CT injection on the central chord.

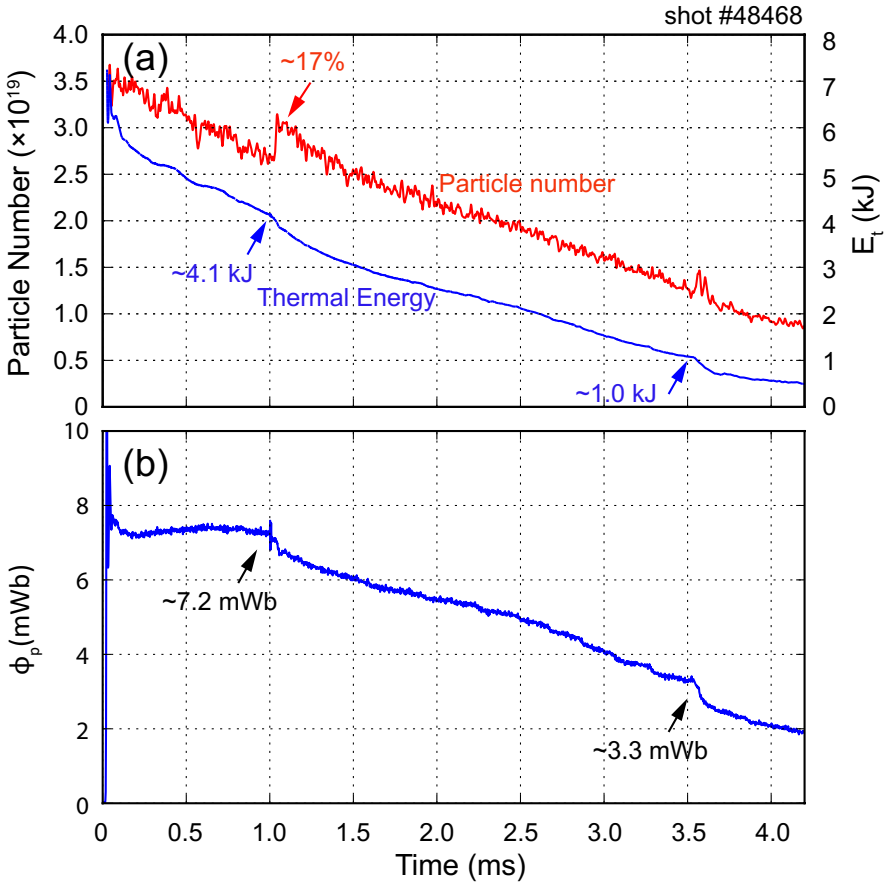

Figure 6.13. Time evolution of the (a) particle number, thermal energy, and (b) flux of FRC. Red line is particle number and blue line is thermal energy. Particle number increased about 17 % after injection of first CT. On the other hand, second CT does not increase the particle number.

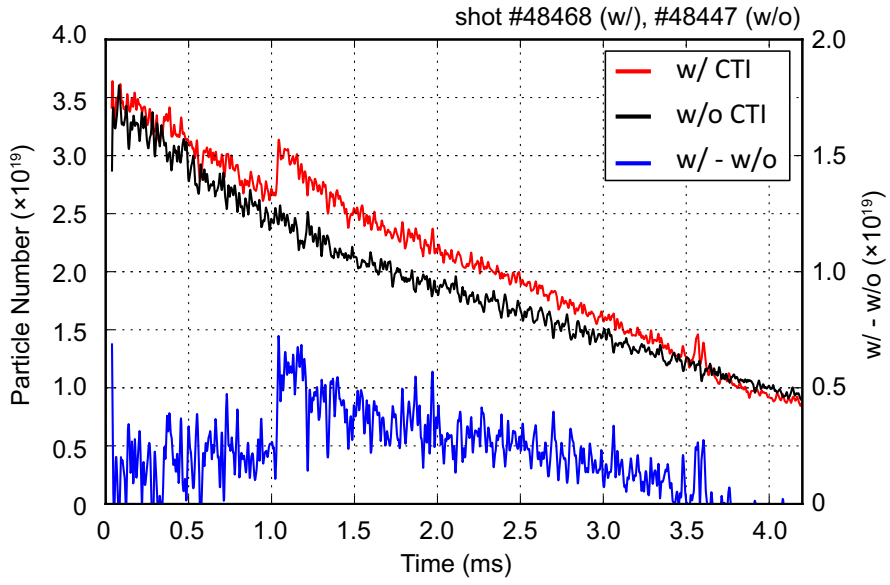

Figure 6.14. Comparison of the particle number with and without CT injection. Red, black, and blue lines are with CTI, without CTI, and difference of particle number (with - without).

6.2.4 Ion Temperature

Figure 6.15 shows the time evolution of the ion temperature at impact position. The CT injected at 1.0 ms from both side, and then it was decreased from around 500 eV to 300 eV. However, the restoring time was $0.5 - 1.0$ ms of time to unalter original temperature rate. The rise time of the temperature correlated with the stabilization time of the magnetic flux, as shown in Fig. 6.10.

On the other hand, the density increased over the 1.0 ms after CT injection. Consequently, it was confirmed that the CT fueled the particles inside the FRC, and then the FRC cooled due to increasing the density, or the CT was cooled FRC because of lower temperature. The rate of decrease in the ion temperature is more conspicuous than the increase in density. Also, the FRC settled to normal FRC behavior about 1.0 ms after particle fueling. In addition, the degree of the rise tends to become late towards the outer shell of the FRC, i.e., the rise time of the ion temperature at the center chord is faster.

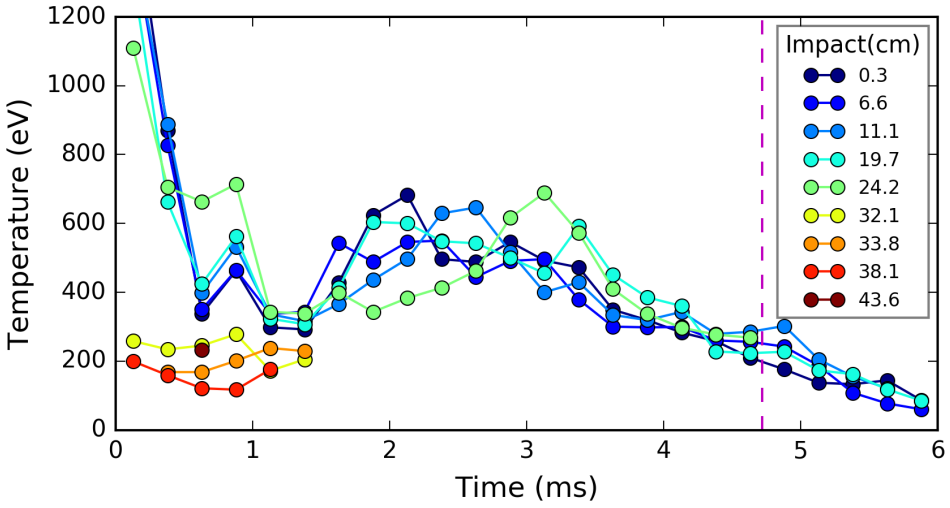

Figure 6.15. Time evolution of ion temperature at impact position.

6.2.5 FRC Global Motion

CT injections from one side and both sides (counter injection) also have been tried and the effect of asymmetrical injection has been investigated.The disruptive effects are minimized when CTs are injected in such a way as to cancel injected azimuthal momentum. Figure 6.16 shows the effect of CT injection on the trajectories of the FRC axis. To estimate the motion of the FRC, the bolometer array at mid-plane used. Figure 6.16(a) is the trajectory on the single side injection case and (b) traces the counter injection case. In the case of single side injection, wobble motion is triggered, and the FRC rotates in the momentum direction of injected CT. To reduce the effect of asymmetrical momentum injection, counter injection has been conducted. In the counter injection case, the wobble motion is not observed because the radial momenta of the 2 CTs is canceled.

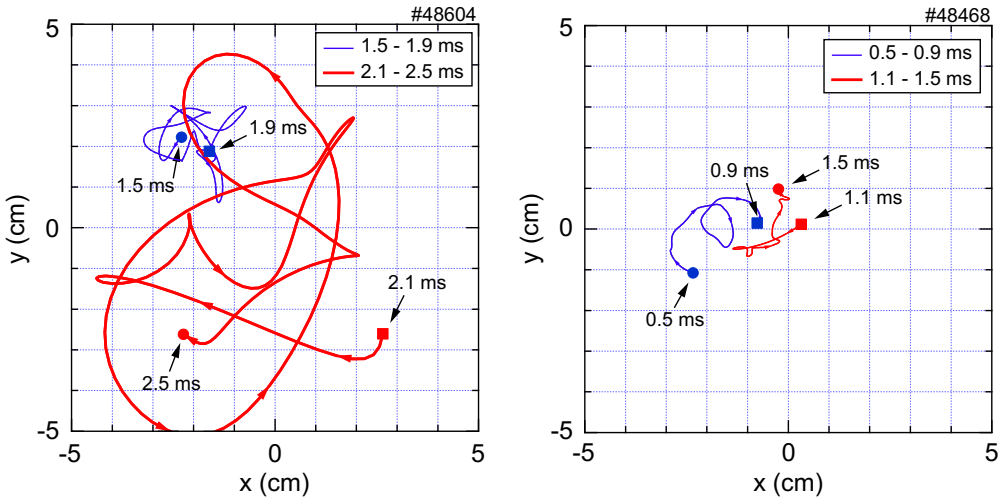

Figure 6.16. Trajectories of the FRC axis before (blue line) and after (red line) CT injection.

6.2.6 D_α Emission and Bremsstrahlung

Figure 6.17 shows the time evolution of the D_α emission on the NC and NE plane. In the case without CT injection, there is a small amount of emission from the FRC after collisional merging formation. However, CT injection cause D_α emission. In general, the CT which is generated by MCPG has a lot of neutral trailing gas. That neutral gas flows into the confinement vessel and comes into with the FRC. Then it increases D_α line emission on the periphery of the FRC . Figure 6.18 shows time evolution of D_α signal at the NC plane and the fast camera images. The fast camera conditions are: the frame rate of 20 kHz and exposure time for each frame is 50 μs. The first CT image shows a domain in which blue and green color are dominant. After CT is injected, the trailing gas enters and touches to the FRC, then neutral gas emits for a few hundred μs or more. This emission is distinct for the first CT sequence. At the second CT injection, the emission from the trajectory of the CT and collided gas are brighter than first CT as shown in the D_α measurement. From this figure 6.17, it is suggested that the neutral gas puffed to generate the first CT reaches the confinement vessel at 2.2 ms and then second the CT excites it. On the NE plane, we can verify the emission of the D_α. From this result, the neutral gas was diffused along the surface of the FRC in both z and theta directions. The second CT image shows a domain in which red color is dominant. This mean that the energy state of the penetrated CT is lower state.

Figure 6.19 shows time evolution of the bremsstrahlung measured on the same plane with D_α. The bremsstrahlung mainly depends on an ion/electron density and an electron temperature, i.e., $I \propto n_e^2/\sqrt{T_e}$, where n_e, and T_e are electron

density, and electron density, respectively. Thereby, the dominant factor of the bremsstrahlung is electron density. In other words, the intensity of bremsstrahlung indicates increased density inside the FRC. The intensity of bremsstrahlung as shown in Fig. 6.19 and the density and particles in Fig. 6.12 and 6.14 are consistent with each other. On the other hand, the bremsstrahlung is not increased at the second CT. Corresponding to this result, the particle number inside the FRC did not increase as shown in Fig. 6.13.

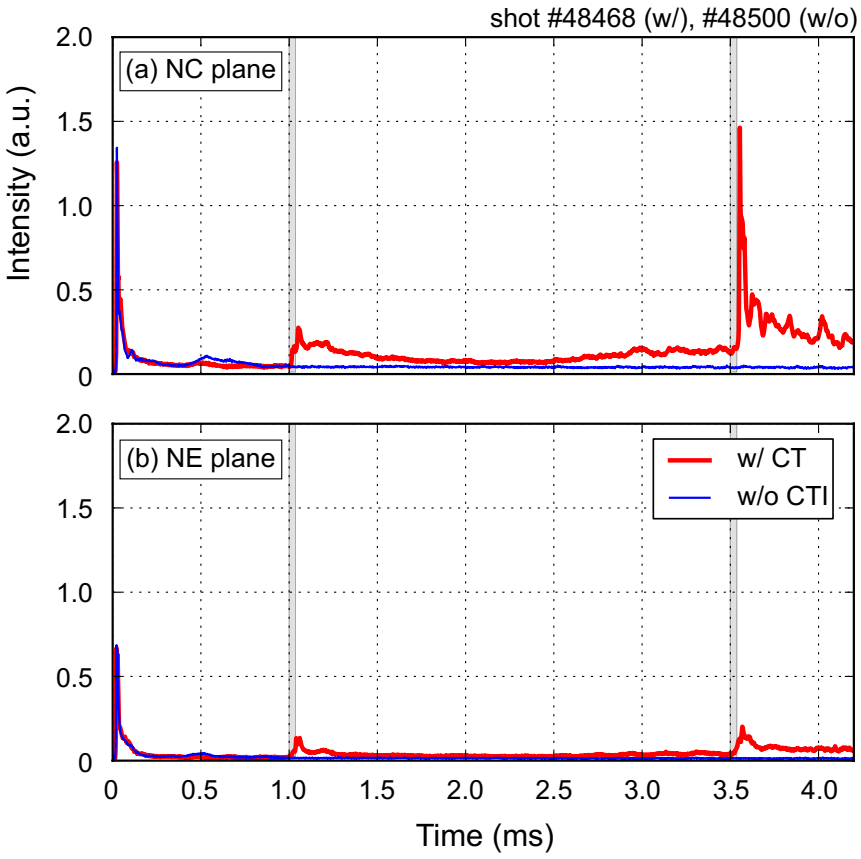

Figure 6.17. Time evolution of the D_α emission on the (a) NC and (b) NE plane. Red line is FRC with CT and blue line is FRC only.

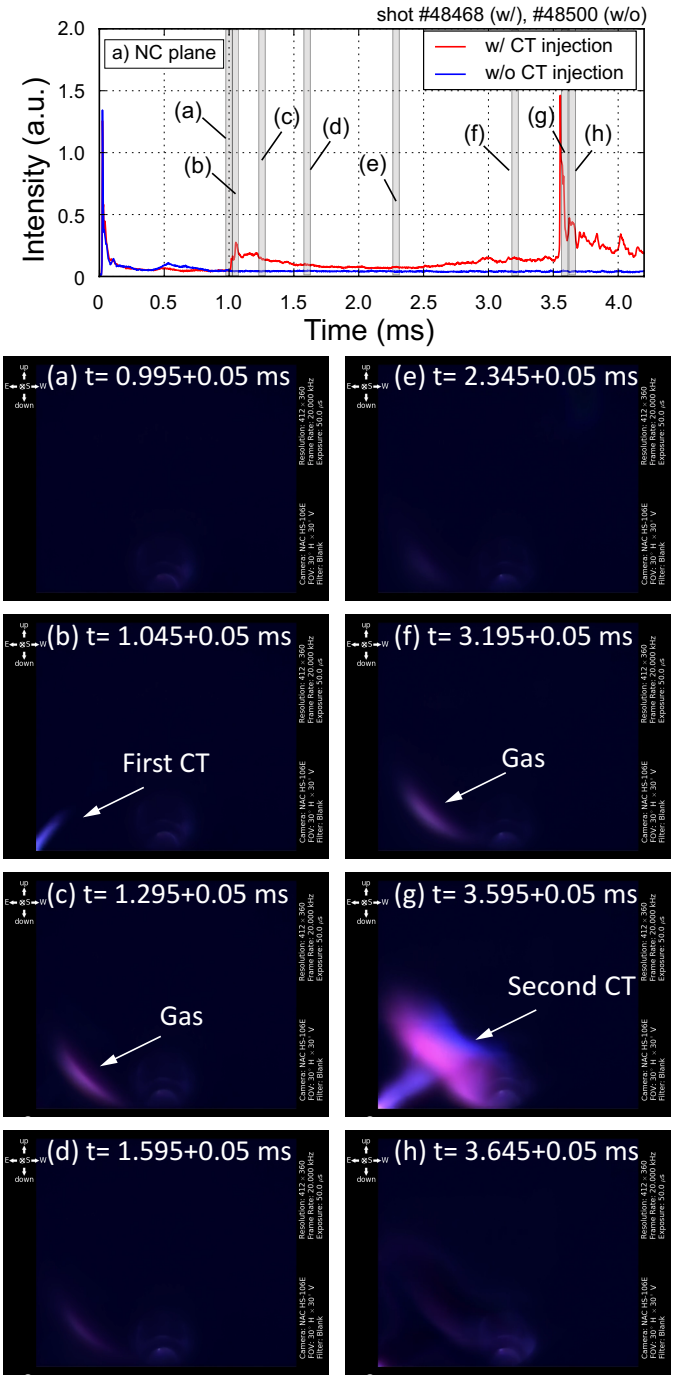

Figure 6.18. Fast-framing camera images of the CT injection. The frame rate is 20 kHz, and the exposure time for each frame is 50 μs.

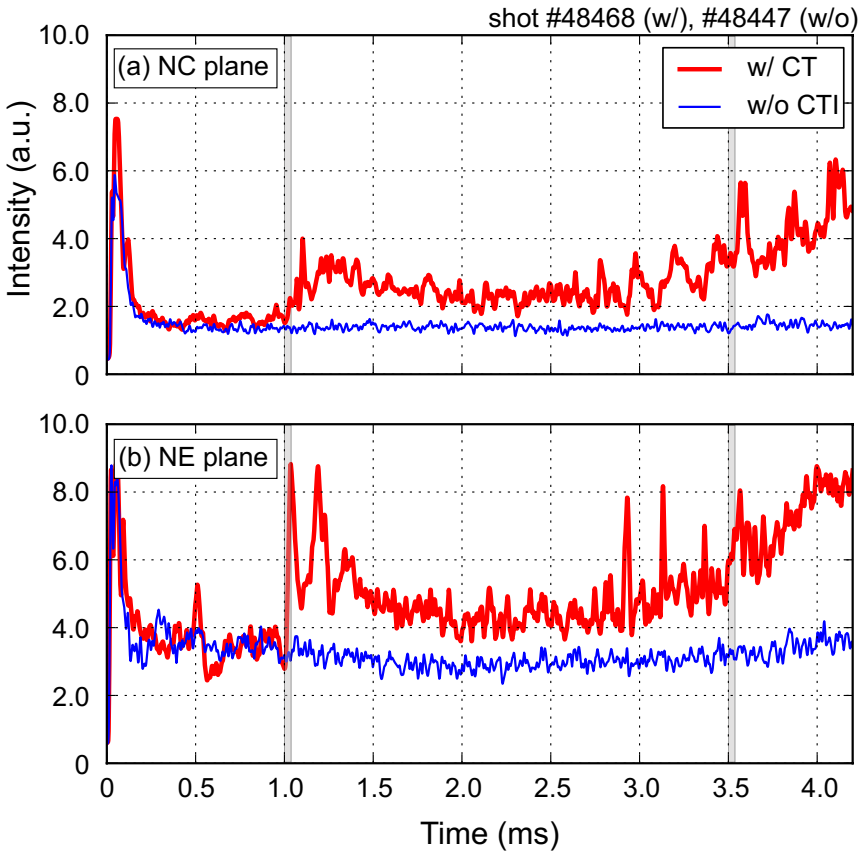

Figure 6.19. Time evolution of the Bremsstrahlung on the (a) NC and (b) NE plane. Red line is FRC with CT and blue line is FRC only.

6.2.7 Effect corresponding to the fast ion

Figure 6.20 shows the time evolution of the neutron signal. The neutron signal is decreased by CT injection quickly. In addition, the separatrix radius started shrinking after the CT injection. But, we did not see the rapid decay of the separatrix radius unlike the neutron signal. Usually, the neutron signal follows the separatrix radius, i.e., the neutron signal is lost when the neutral beam is terminated or FRC is dies. However, a shape of the FRC is maintained even after CT injection. So, the CT might have disrupted the fast ions. Thus the pressure balance which surround the FRC was lost. Confinement time τ of the fast beam

ion depends on electron temperature and electron density, i.e. $\tau \propto T_e/n_e$. In other words, the fast ions were decayed by cooling and increase of electron density in the FRC.

Additionally, the fast ion will be decayed by a charge-exchange with neutral gas which is poured into CT injector to begin the breakdown. The injected neutral gas will be spread surround the FRC, and then the fast ion which has large Larmor radius hits with neutral gas. Therefore, the neutron signal started decaying, and pressure balance around the FRC changed.

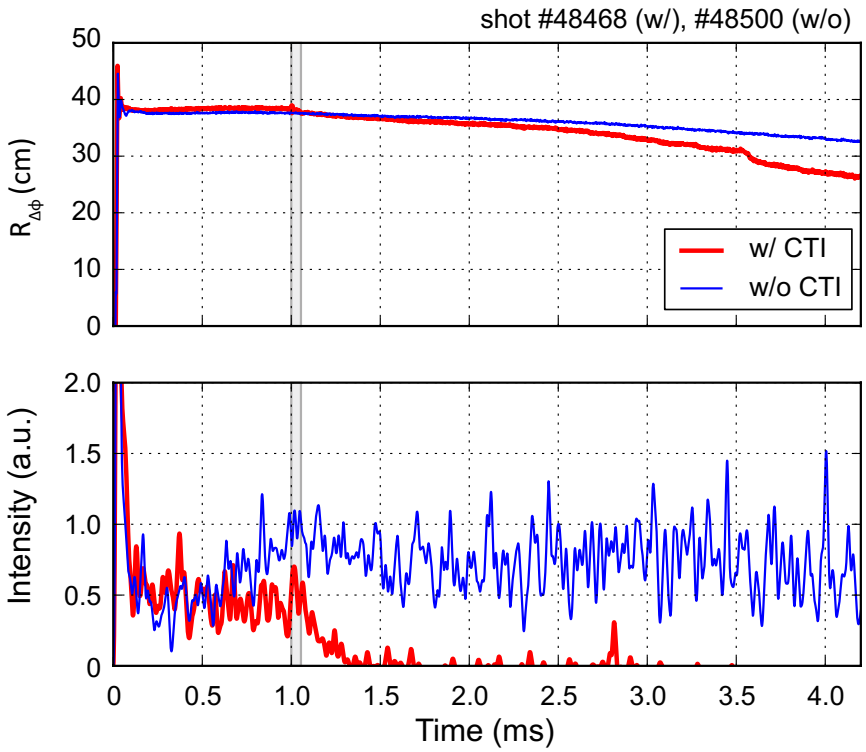

Figure 6.20. Time evolution of the neutron signal. The neutron radiation is lost by CT injection at 1 ms.

6.2.8 Deposit Neutral Beam Power into FRC

As mentioned in the introduction, the neutral beam power is necessary deposited to make as much as incident as possible. To estimate the deposition rate, the shine-through measurement use [14].

Figure 6.21 shows a shine-through detection for each NBs. These signals are normalized by the value before FRC merging. As mentioned above, a shine-through affect density and temperature of the core plasma. After colliding the FRCs, the shine-through decrease in order to deposit the NB power into the FRC. At 1.0 ms, the shine-through rate was decreased by increasing the density. After that, the signal remains reduced. That is, we succeeded in injecting more energy for a long time. As a result, it is presumed that it is possible to increase the beam energy. The neutral beam power can increase by the ramp up the acceleration voltage for the beam, then the current becomes easily increasable, i.e., the input energy increase. Thereby, the neutral beam can deposit more energy to FRC. In other words, a high power can be supplied with NBI of the same port area.

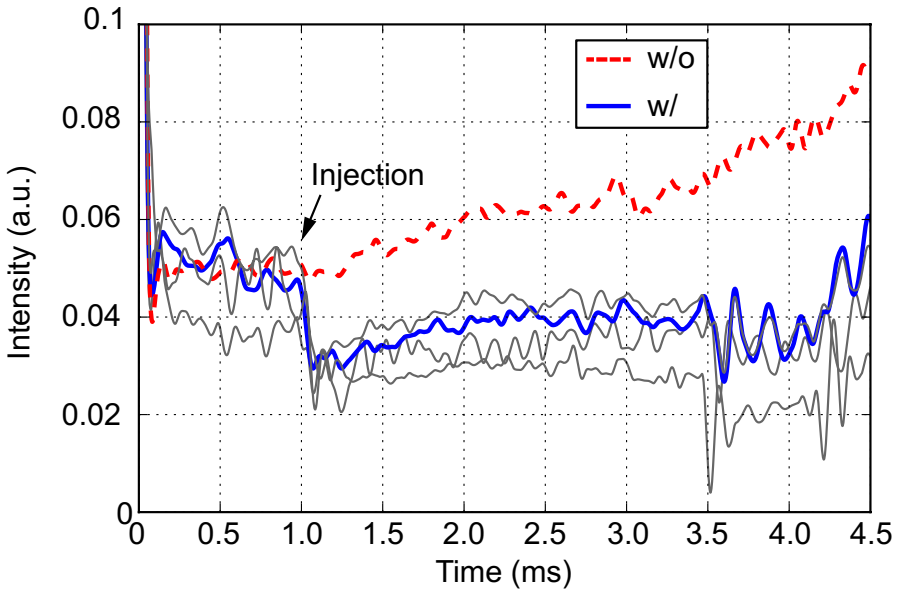

Figure 6.21. Time evolution of intensity of shine-through of neutral beams. CT injected at 2 ms. Red (dashed line) and Blue (solid line) are w/o CT and w/ CT case, respectively. These lines are NB source NB2, and gray lines are another NB's signals. The intensity is decreased after injection. This means that the NB power was deposited into FRC. Then shine-through dropped

6.2.9 Shine-Through Rate

The measurement path of the shine-through is similar with density measurement by interferometer. As shown previous section, both measurement items across around the center of FRC. Since this location, these signals can evaluate as an FRC's behavior. As a role of these diagnostics, the CO_2 laser interferometry can measure an FRC's density. On the other hand, the shine-through measurement can measure the proportion of particles that did not ionize. However, it is difficult to estimate the behavior of an FRC by shine-through measurement because this measurement includes some plasma parameters, such as density. The interferometry can measure the plasma density only. Thus it will can estimate the cause of variation in a decreasing and increasing rate of shine-through.

The variation of the density is changed when the FRC shrink varied with time. When the CT penetrated FRC, the line-integrated density increased, as shown in Fig. 6.12. In addition, the shine-through rate decreased, as shown in Fig. 6.21. In the previous section, we described that injection energy from neutral beams deposited into the FRC due to increment of density. A sine-through rate will be determined by a density distribution inside of FRC. The interferometry is determined by FRC's density, surrounded density of FRC is smaller than inside FRC. Therefore, we will use both measurement to assess the behavior of FRC.

Figure 6.22 shows a comparison between $n_e dl$ and shine-through rate. The increasing rate of the $n_e dl$ is 18%, and the decreasing rate of the shine-through is 38% after CT injection. To define the time constant τ of $n_e dl$ and shine through rate after CT injection at 1.0 ms, we assumed that both waveform will be decayed exponentially $y = y_0 + Aexp\left\{-\frac{x-x_0}{\tau}\right\}$, then the time constant τ are; $\tau_{n_e dl}$ is 0.47 ms and τ_{st} is 0.59 ms, where $\tau_{n_e dl}$ is time constant of $n_e dl$ and τ_{st} is time constant of shine-through. From this result, increment of ionization rate is considered as an effect by increasing a density.

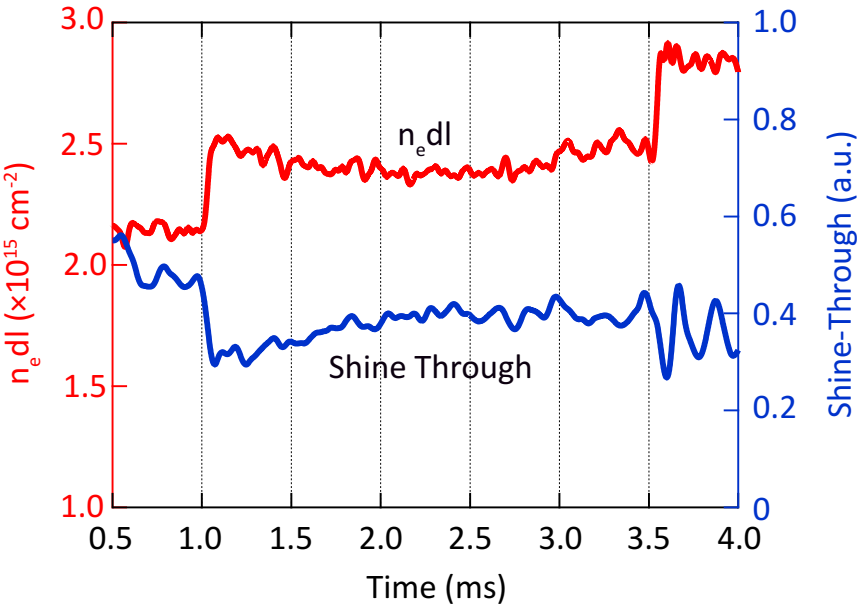

Figure 6.22. Comparison between line-integrated electron density and rate of shine-through.

Chapter 7

Upgrade of the CT Injector

As shown in section 6.2, the CT can fuel the particles into the FRC with particles. However, the trailing gas, which follows the penetrated CT, flows into the confinement vessel and potentially cools the FRC plasma. In order to decrease this trailing neutral gas from the CT injector, we have been developed the Pre-Ionization (PI) technique. The concept of this technique is similar with Pulsed-Plasma Thruster (PPT), also know as a plasma jet engine [11]. The discharging electrode is made of semi-rigid coaxial cable with teflon insulator. The material of the inner and outer electrodes are copper and the diameter of the outer electrode is 6.5 mm. The initial plasma discharge is initiated between electrodes with an arc across the insulator. The maximum charging voltage is 10 kV. Then it assists the breakdown of the CT injector. Thus, the amount of initial neutral gas can be reduced. Figure 7.1 shows (a) the PI source on the CT injector and (b) cross-section of the PI source. The outer electrode of PI is grounded through the outer electrode of the CT injector. The plasma generated by PI is accelerated by Lorentz-force and then filled neutral gas is ionized localy.

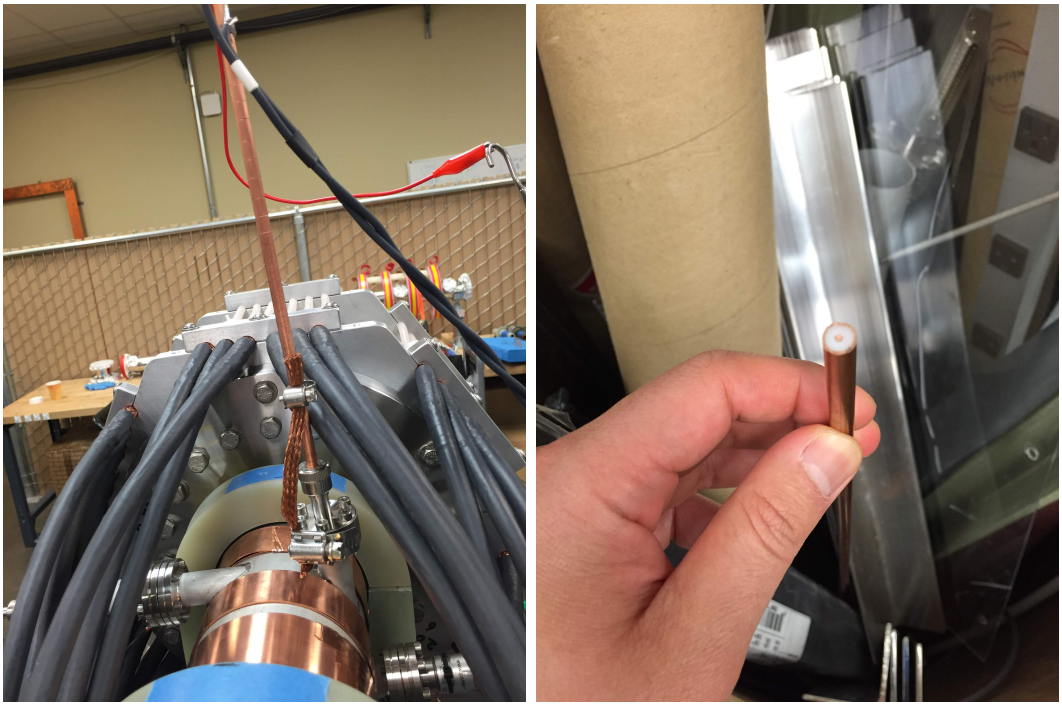

(a) (b)

Figure 7.1. Picture of the PI source on the CT injector. (a) Installation of the PI source and (b) cross-section of the PI.

7.1 Effect of PI on Gun Voltage

Figure 7.2 shows the discharge voltage with and without PI. The PI started 20 μs before gun discharge. In the case without PI, the breakdown is delayed about 1 μs. On the other hand, the breakdown with PI is initiated just after triggering of the main bank. So, this suggests that the initial gas pressure to start the breakdown can be decreased. By using this technique, we can operate the injector with the lower initial gas pressure.

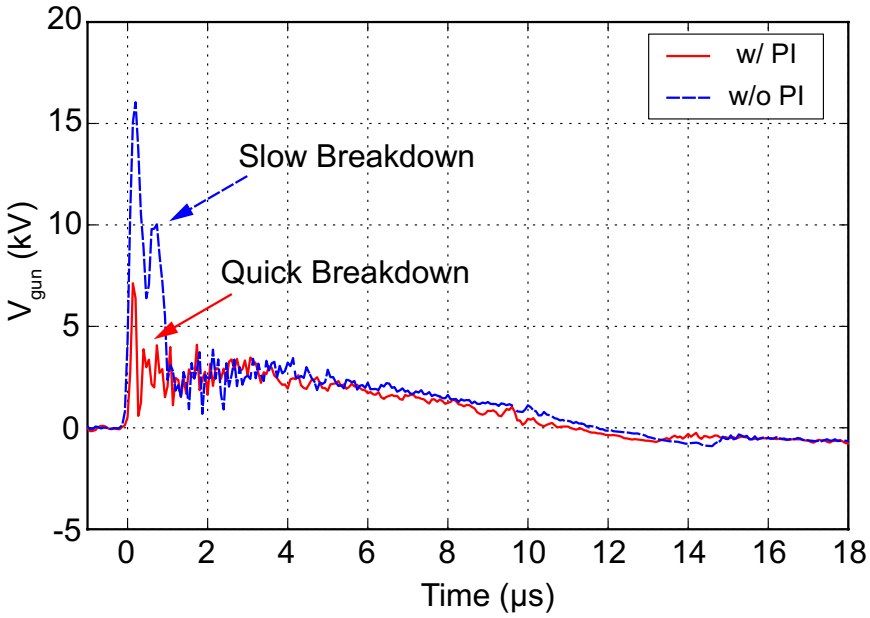

Figure 7.2. Comparison of the gun voltage with and without PI.The solid line is with PI, and the dotted line is without PI. Initially filled gas pressure is also same in those case. The breakdown is faster with PI.

7.2 Comparison of Light Emission on the Glass Chamber

Figure 7.3 shows time evolution of light emission in the glass tube with 40 psia, 30 psia, and 25 psia initial gas fill. Usually, developed CT injector is filled with 40 psia of initial gas pressure because 30 psia is hard to breakdown. A traveling CT emits the large pulse between $28 - 35$ μs, as shown in Fig. 7.3. Following the signal by CT, is the trailing gas. The emission of the trailing gas under the 40 psia is higher than 30 psia and 25 psia. As a result, the amount of trailing gas can be easily controled and decreased by using the PI technique.

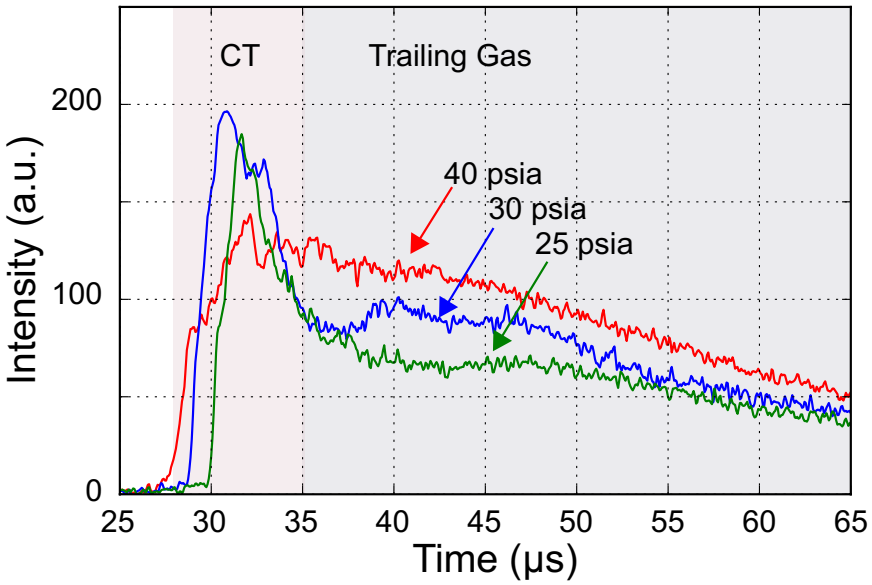

Figure 7.3. Comparison of the PMT signal on the glass tube between 40 psia, 30 psia, and 25 psia.

7.3 Result of CT Injection with PI source

The PI source was mounted on the South East CT injector for the test injection with pre-ionization source. In this section the primary result of the CT injection with PI system is described. In this series of experiments, a CT is injected at 3.5 ms from SC CT injector. Figure 7.4 shows the time evolution of the geometry of the FRC: separatrix radius, length, and volume. There is no apparent change in the global structure of the FRC compared to the case without PI. The line-integrated electron density is increased on the center chord, and the particle number is increased 12% by CT injection, as shown in Fig. 7.5 and 7.6. That increased particle number is approximately 1×10^{18}. On the other had, the flux was decreased after CT injection as seen on the case without PI. However, the separatrix radius did not

experience the same stair-like drop. Intensity of Dα emission is lower compared to the the case without PI as shown in Fig. 7.7. So, this suggests that the trailing neutral gas is significantly smaller than the case without PI. Figure 7.8 shows the bremsstrahlung emission. The bremsstrahlung emission is slightly increased at NE plane as refueling increases particle number. But the increase was not as dramatic as in the case without PI. Figure 7.9 shows the comparison of the neutron signal between the cases with/without PI. The neutron signal without PI is decreased quickly after injection. On the other hand, no changes are seen in case with PI. Also the decay time is changed slowly after CT injection. As mentioned above the trailing gas is reduced by using PI technique.

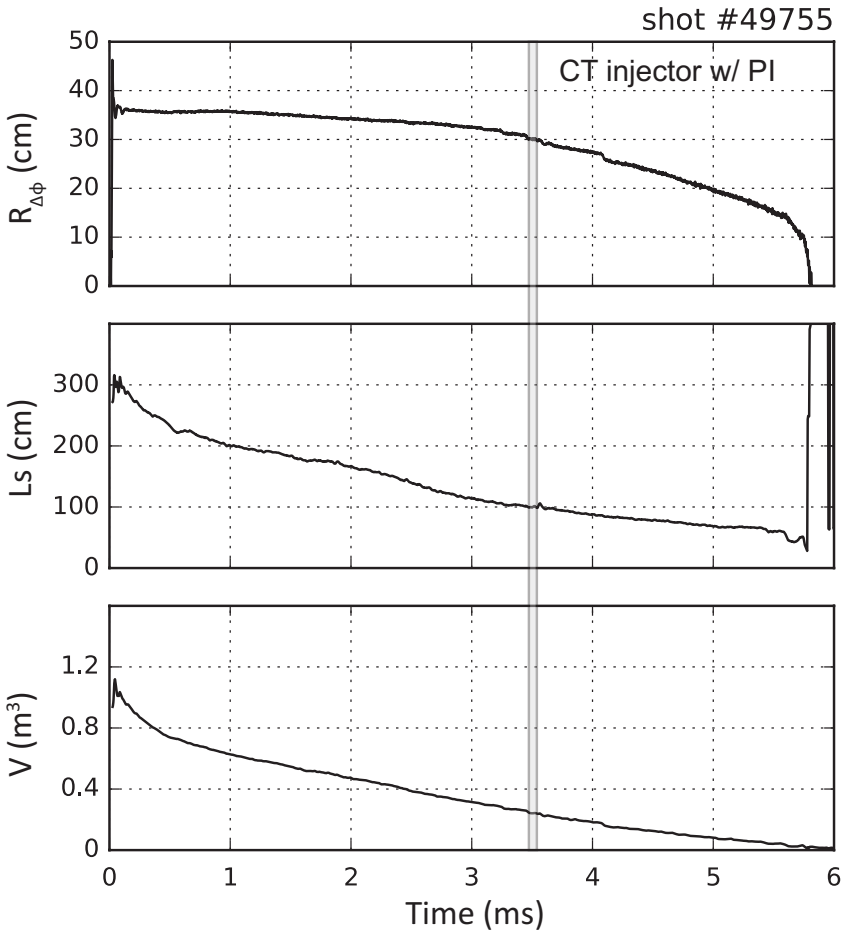

Figure 7.4. Time evolution of FRC geometry: separatrix radius, length, and volume. The CT injection was 3.5 ms.

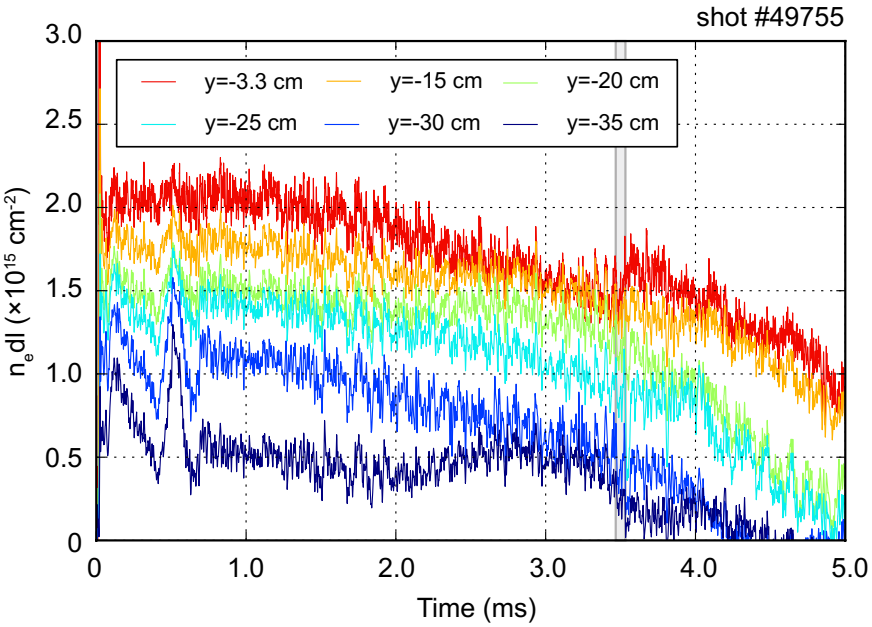

Figure 7.5. Time evolution of the line-integrated electron density of each chord: y = -3.3, -15, -20, -25, -30 and -35 cm. Line-density measured by chords around center (-3.3 and -15 cm) are increased at injection timing and maintain the higher density. On the other hand, there are no significant change in outer chords. after CT injection.

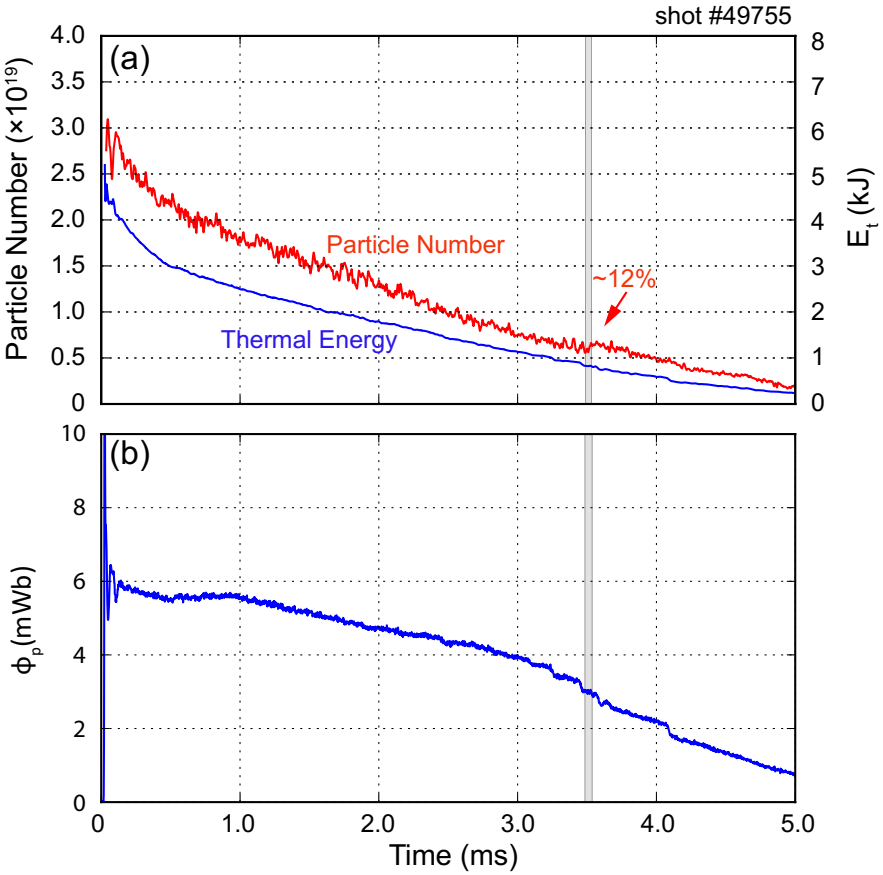

Figure 7.6. Time evolution of the (a) particle number, thermal energy, and (b) flux of FRC. Red line is particle number and blue line is thermal energy. particle number was increased about 12% after injection at first CT.

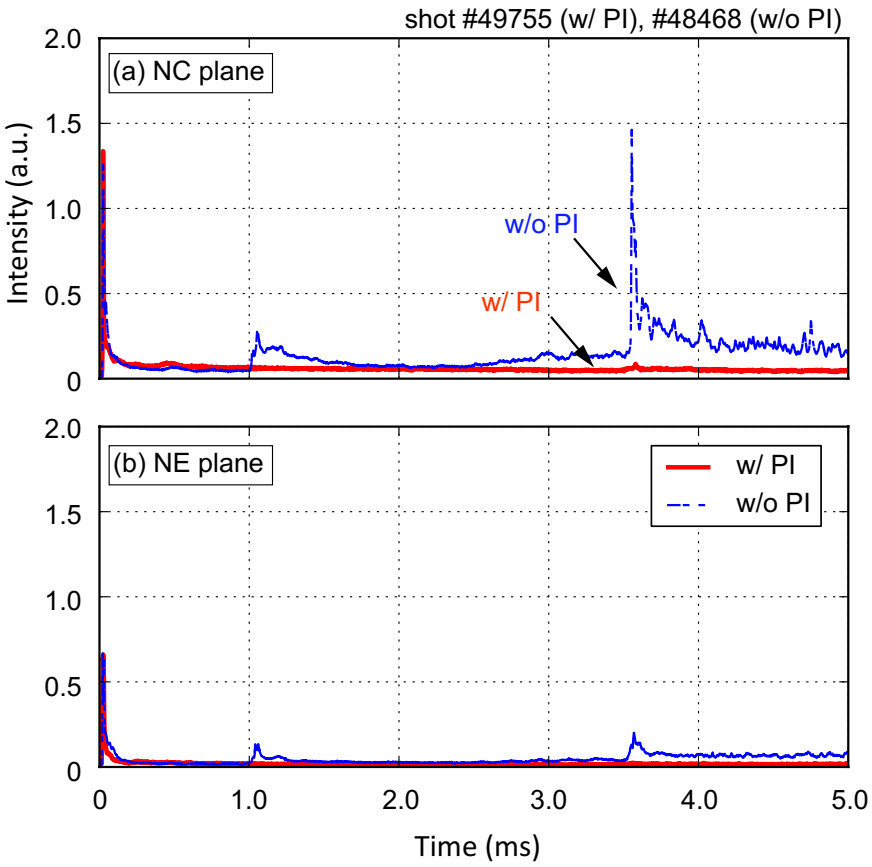

Figure 7.7. Time evolution of the Dα emission on the (a) NC and (b) NE plane. Red line is FRC with PI and blue line is without PI. The neutral gas does not flow inside the confinement vessel.

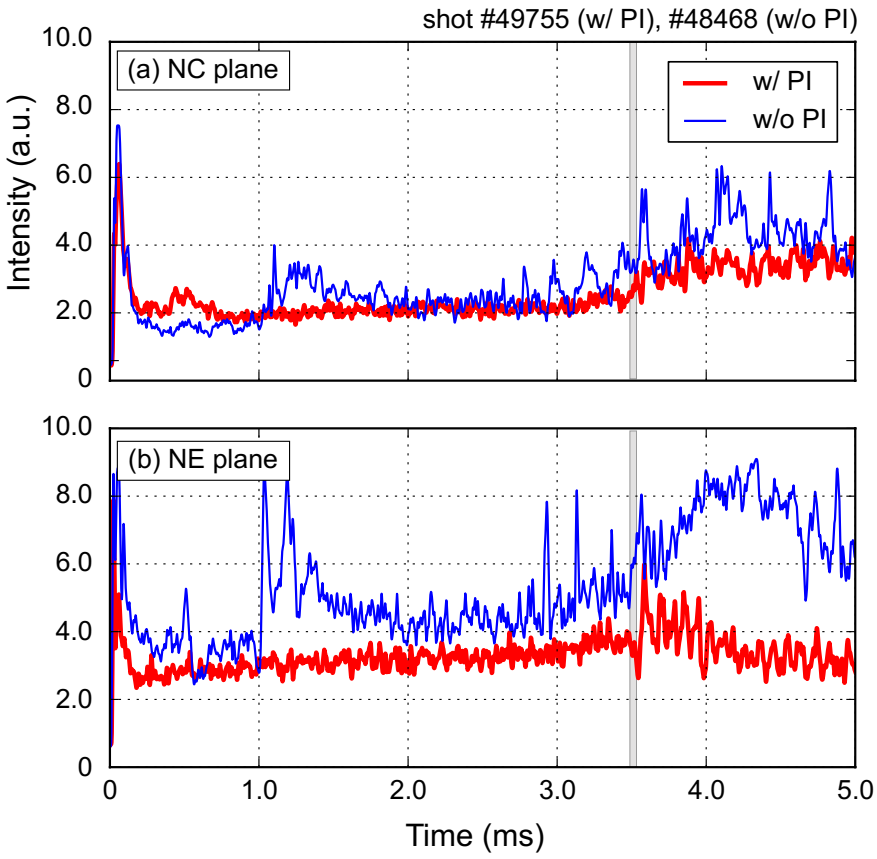

Figure 7.8. Time evolution of the Bremsstrahlung emission on the (a) NC and (b) NE plane. Both case are injected CT. Red line is CT with PI and blue line CT without PI.

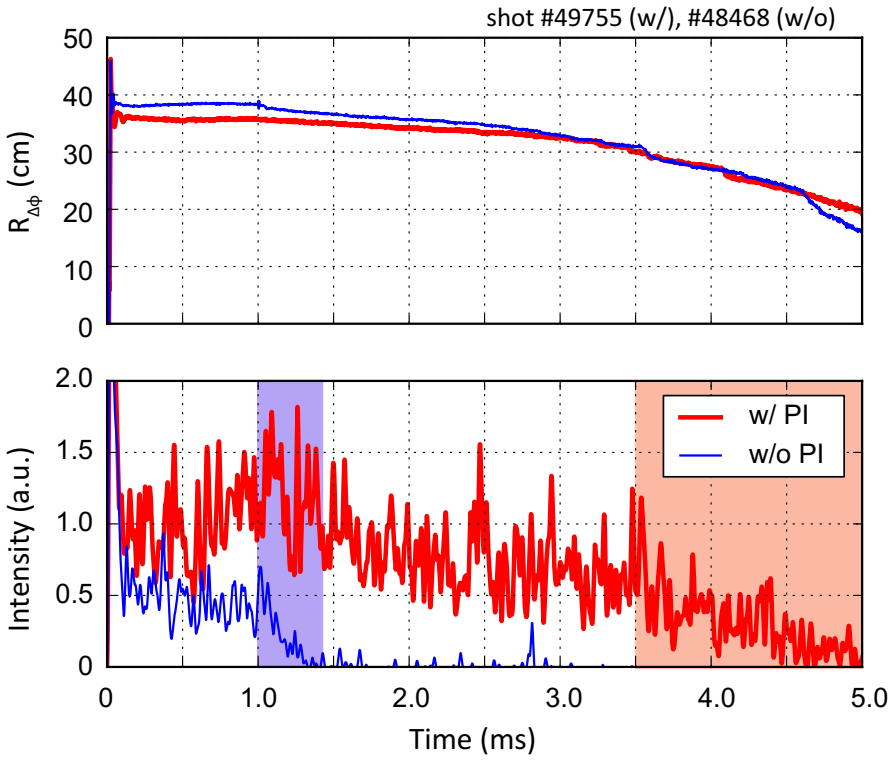

Figure 7.9. Time evolution of the neutron signal. The neutron radiation is not lost by CT injection with PI at 3.5 ms. The filled region means the decay time of the neutron signal after injection. In case of the with PI, the decay time is longer than the case without PI.

Chapter 8

Summary

A compact toroid injector developed for the FRC plasma at Tri Alpha Energy, which is the largest in the world. The C-2U FRC device has achieved over 10 ms by neutral beam injection and heating. The role of neutral beam injection is an injection of neutral particles with 15 keV. Therefore, an energy confinement time of FRC extended and improved confinement condition. However, it is not enough just to fuel the particles for FRC. Thus the particle refueling technique is most important to extend the lifetime. Hence we have started developing compact toroid injector system. The result describes as below.

1. **Development of CT injector**

   We developed a compact toroid (CT) injector as a original model for particle refueling to FRC device. The dimension of the CT injector are; the diameter of outer and inner electrode are 83.1 mm as an inner diameter and 54 mm as an outer diameter, respectively. The achieved parameters are as follows: velocity ~ 100 km/s, electron temperature $20-40$ eV, electron den-

sity $\sim 1.9 \times 10^{15}\mathrm{cm}^{-3}$, and mass of CT ~ 12 μg. The required energy to penetrate/inject to FRC is 4 kJ/m^3, and the actual CT's energy was over 20 kJ/m^3. Also, the multi-pulse circuit had been developed to increase a number of CTs. The repetition rate is up to 1 kHz, which is the fastest repeatability in the world. Therefore, the CT injector can inject up to 3 CTs.

2. **Result of CT Injection into FRC**

   The two CT injectors installed onto the confinement vessel on the C-2/C-2U device and a multi-pulse system mounted on one side. Also, the CTs can control independently. As a result of single side injection, the particles inventory increased. However, the wobble motion was triggered due to injection of the CT's momentum. On the other contrary, when the CT injects from both side at the same time, there was no significant motion such as wobble motion because the momentum was canceled. In the case of the counter CT injection, the particle inventory increased 20% at injected time. Moreover, the decaying rate of the poloidal flux was accelerated at CT injection time because the toroidal current decreased by increasing the particle inventory. Moreover, the transmission light of the shine-through rate was reduced, i.e., the NB power more deposited inside the FRC.

3. **Improved Pre-Ionization Technique**

   Actual CT injection follows the neutral gas as a trailing gas after CT injected. The flowed neutral gas surround and touch with FRC, and then the FRC was

cooled. Also, the fast ions disappeared. To reduce the surrounding neutral gas, we developed the pre-ionization system. This system includes semi-rigid cable and fast bank, which is lower capacitance with 10 kV. The principle of this technique is similar to pulsed-plasma thruster (PPT), and a breakdown is easier because a Teflon is used to breakdown between electrodes of the semi-rigid cable. As a result, a puffed gas pressure reduced from 40 psia to 25 psia. Therefore, the following neutral gas was reduced significantly. Consequently, the hot gas signal inside the confinement vessel was decreased and disappeared. In addition, a neutron signal did not disappear, and it was not shown a disruption by CT injection. Moreover, the CT with PI augmented particle inventory about 10%.

Bibliography

[1] I. A. E. Agency, *ITER interim design report package documents*, ITER EDA documentation series, International Atomic Energy Agency, 1996.

[2] W. T. Armstrong, R. K. Linford, J. Lipson, D. A. Platts et E. G. Sherwood, *Field- reversed experiments (FRX) on compact toroids*, The Physics of Fluids, 24 (1981), p. 2068–2089.

[3] C. W. Barnes, J. C. Fernández, I. Henins, H. W. Hoida, T. R. Jarboe, S. O. Knox, G. J. Marklin et K. F. McKenna, *Experimental determination of the conservation of magnetic helicity from the balance between source and spheromak*, The Physics of Fluids, 29 (1986), p. 3415–3432.

[4] C. W. Barnes, T. R. Jarboe, G. J. Marklin, S. O. Knox et I. Henins, *The impedance and energy efficiency of a coaxial magnetized plasma source used for spheromak formation and sustainment*, Physics of Fluids B: Plasma Physics, 2 (1990), p. 1871–1888.

[5] P. M. Bellan, *Spheromaks: A Practical Application of Magnetohydrodynamic Dynamos and Plasma Self-Organization*, 2000.

[6] M. W. Binderbauer, H. Y. Guo, M. Tuszewski, S. Putvinski, L. Sevier, D. Barnes, N. Rostoker, M. G. Anderson, R. Andow, L. Bonelli, F. Brandi, R. Brown, D. Q. Bui, V. Bystritskii, F. Ceccherini, R. Clary, A. H. Cheung, K. D. Conroy, B. H. Deng, S. A. Dettrick, J. D. Douglass, P. Feng, L. Galeotti, E. Garate, F. Giammanco, F. J. Glass, O. Gornostaeva, H. Gota, D. Gupta, S. Gupta, J. S. Kinley, K. Knapp, S. Korepanov, M. Hollins, I. Isakov, V. A. Jose, X. L. Li, Y. Luo, P. Marsili, R. Mendoza, M. Meekins, Y. Mok, A. Necas, E. Paganini, F. Pegoraro, R. Pousa-Hijos, S. Primavera, E. Ruskov, A. Qerushi, L. Schmitz, J. H. Schroeder, A. Sibley, A. Smirnov, Y. Song, X. Sun, M. C. Thompson, A. D. Van Drie, J. K. Walters et M. D. Wyman, *Dynamic Formation of a Hot Field Reversed Configuration with Improved Confinement by Supersonic Merging of Two Colliding High-{\&beta} Compact Toroids*, Phys. Rev. Lett., 105 (2010), p 45003.

[7] M. W. Binderbauer, T. Tajima, L. C. Steinhauer, E. Garate, M. Tuszewski, L. Schmitz, H. Y. Guo, A. Smirnov, H. Gota, D. Barnes, B. H. Deng, M. C. Thompson, E. Trask, X. Yang, S. Putvinski, N. Rostoker, R. Andow, S. Aefsky, N. Bolte, D. Q. Bui, F. Ceccherini, R. Clary, A. H. Cheung, K. D. Conroy, S. A. Dettrick, J. D. Douglass, P. Feng, L. Galeotti, F. Giammanco, E. Granstedt, D. Gupta, S. Gupta, A. A. Ivanov, J. S. Kinley, K. Knapp, S. Korepanov, M. Hollins, R. Magee, R. Mendoza, Y. Mok, A. Necas, S. Primavera, M. Onofri, D. Osin, N. Rath, T. Roche, J. Romero, J. H. Schroeder, L. Sevier, A. Sibley, Y. Song, A. D. V. Drie, J. K. Walters, W. Waggoner, P. Yushmanov et K. Zhai, *A high performance field-reversed configuration*, Physics of Plasmas, 22 (2015), p 56110.

[8] M. W. Binderbauer, T. Tajima, M. Tuszewski, L. Schmitz, A. Smirnov, H. Gota, E. Garate, D. Barnes, B. H. Deng, E. Trask, X. Yang, S. Putvinski, R. Andow, N. Bolte, D. Q. Bui, F. Ceccherini, R. Clary, A. H. Cheung, K. D. Conroy, S. A. Dettrick, J. D. Douglass, P. Feng, L. Galeotti, F. Giammanco, E. Granstedt, D. Gupta, S. Gupta, A. A. Ivanov, J. S. Kinley, K. Knapp, S. Korepanov, M. Hollins, R. Magee, R. Mendoza, Y. Mok, A. Necas, S. Primavera, M. Onofri, D. Osin, N. Rath, T. Roche, J. Romero, J. H. Schroeder, L. Sevier, A. Sibley, Y. Song, L. C. Steinhauer, M. C. Thompson, A. D. V. Drie, J. K. Walters, W. Waggoner, P. Yushmanov et K. Zhai, *Recent breakthroughs on C-2U: Norman's legacy*, AIP Conference Proceedings, 1721 (2016), p 30003.

[9] M. R. Brown, D. M. Cutrer et P. M. Bellan, *Motion and equilibrium of a spheromak in a toroidal flux conserver*, Physics of Fluids B: Plasma Physics, 3 (1991), p. 1198–1213.

[10] M. R. Brown, A. D. B. III et P. M. Bellan, *Characterization of a spheromak plasma gun: The effect of refractory electrode coatings*, Journal of Applied Physics, 69 (1991), p. 6302–6312.

[11] R. L. Burton et P. J. Turchi, *Pulsed Plasma Thruster*, Journal of Propulsion and Power, 14 (1998), p. 716–735.

[12] R. E. Chrien et S. Okada, *Field- reversed configuration profiles and resistivities inferred from the radial line- integral density profile*, The Physics of Fluids, 30 (1987), p. 3574–3578.

[13] R. Clary, A. Roquemore, J. Douglass, D. Jaramillo, S. Korepanov, R. Magee, S. Medley et A. Smirnov, *A mass resolved, high resolution neutral particle analyzer for C-2U*, Review of Scientific Instruments, 87 (2016), p 11E703.

[14] J. H. Foote, A. W. Molvik et W. C. Turner, *Plasma measurements from neutral- beam attenuation*, Review of Scientific Instruments, 54 (1983), p. 928–934.

[15] O. Gornostaeva, B. H. Deng, E. Garate, H. Gota, J. Kinley, J. Schroeder et M. Tuszewski, *Two-color CO2/HeNe laser interferometer for C-2 experiment*, Review of Scientific Instruments, 81 (2010), p 10D516.

[16] D. K. Gupta, E. Paganini, A. Balvis, L. Bonelli, B. H. Deng, F. Giammanco, O. Gornostaeva, R. Hayashi, K. Knapp, P. Marsili, M. McKenzie, R. Pousa-Hijos, S. Primavera, J. Schroeder et M. Tuszewski, *Doppler spectroscopy and D-alpha emission diagnostics for the C-2 FRC plasma*, Review of Scientific Instruments, 81 (2010), p 10D737.

[17] J. H. Hammer, J. L. Eddleman, C. W. Hartman, H. S. McLean et A. W. Molvik, *Experimental demonstration of compact torus compression and acceleration*, Physics of Fluids B: Plasma Physics, 3 (1991), p. 2236–2240.

[18] J. H. Hammer, C. W. Hartman, J. L. Eddleman et H. S. McLean, *Experimental Demonstration of Acceleration and Focusing of Magnetically Confined Plasma Rings*, Phys. Rev. Lett., 61 (1988), p. 2843–2846.

[19] A. E. D. Heylen, *Electrical ionisation and breakdown of gases in a crossed magnetic field*, IEE Proceedings A Physical Science, Measurement and Instrumentation, Management and Education, Reviews, 127 (1980), p 221.

[20] A. L. Hoffman, R. D. Milroy et L. C. Steinhauer, *Poloidal flux loss in a field- reversed theta pinch*, Applied Physics Letters, 41 (1982), p. 31–33.

[21] D. L. Jassby, *Neutral-beam-driven tokamak fusion reactors*, Nuclear Fusion, 17 (1977), p 309.

[22] A. Komori, N. Ohyabu, H. Yamada, O. Kaneko, K. Kawahata, K. Ida, Y. Nakamura, T. Akiyama, N. Ashikawa, M. Emoto, H. Funaba, P. Goncharov, M. Goto, H. Idei, K. Ikeda, S. Inagaki, M. Isobe, H. Kawazome, K. Khlopenkov, T. Kobuchi, A. Kostrioukov, S. Kubo, R. Kumazawa, Y. Liang, S. Masuzaki, T. Minami, J. Miyazawa, T. Morisaki, S. Morita, S. Murakami, S. Muto, T. Mutoh, Y. Nagayama, H. Nakanishi, K. Narihara, Y. Narushima, K. Nishimura, N. Noda, T. Notake, H. Nozato, S. Ohdachi, Y. Oka, M. Osakabe, T. Ozaki, B. J. Peterson, A. Sagara, T. Saida, K. Saito, S. Sakakibara, R. Sakamoto, M. Sasao, K. Sato, M. Sato, T. Seki, T. Shimozuma, M. Shoji, H. Suzuki, Y. Takeiri, N. Takeuchi, N. Tamura, K. Tanaka, K. Toi, T. Tokuzawa, Y. Torii, K. Tsumori, K. Y. Watanabe, T. Watari, Y. Xu, I. Yamada, S. Yamamoto, T. Yamamoto, M. Yokoyama, Y. Yoshimura, M. Yoshinuma, K. Itoh, K. Matsuoka, K. Ohkubo,

T. Satow, S. Sudo, T. Uda, K. Yamazaki, O. Motojima et M. Fujiwara, *Recent results from the Large Helical Device*, Plasma Physics and Controlled Fusion, 45 (2003), p 671.

[23] S. Korepanov, A. Smirnov, R. Clary, S. Dettrick, P. Deichuli, A. Kondakov et S. Murakhtin, *Modulated active charge exchange fast ion diagnostic for the C-2 field-reversed configuration experiment*, Review of Scientific Instruments, 83 (2012), p 10D720.

[24] N. A. Krall, *The effect of low- frequency turbulence on flux, particle, and energy confinement in a field- reversed configuration*, Physics of Fluids B: Plasma Physics, 1 (1989), p. 1811–1817.

[25] P. T. Lang et E. al., *High-Efficiency Plasma Refuelling by Pellet Injection from the Magnetic High-Field Side into ASDEX Upgrade*, Phys. Rev. Lett., 79 (1997), p. 1487–1490.

[26] T. Matsumoto, J. Sekiguchi, T. Asai, H. Gota, E. Garate, I. Allfrey, T. Valentine, M. Morehouse, T. Roche, J. Kinley, S. Aefsky, M. Cordero, W. Waggoner, M. Binderbauer et T. Tajima, *Development of a magnetized coaxial plasma gun for compact toroid injection into the C-2 field-reversed configuration device*, Review of Scientific Instruments, 87 (2016), p 53512.

[27] H. S. McLean, I. L. Eddleman, J. H. Hammer, C. W. Hartman et A. W. Molvik, *Ring Accelerator Experiment (RACE)*, *in* IEEE Conference Record - Abstracts. 1991 IEEE International Conference on Plasma Science, 1991, p 166.

[28] T. Ogawa, N. Fukumoto, M. Nagata, H. Ogawa, M. Maeno, K. Hasegawa, T. Shibata, T. Uyama, J. Miyazawa, S. Kasai, H. Kawashima, Y. Miura, S. Sengoku, H. Kimura et J.-M. Group, *Compact toroid injection experiment in JFT-2M*, Nuclear Fusion, 39 (1999), p 1911.

[29] T. Onchi, D. McColl, A. Rohollahi, C. Xiao, A. Hirose, M. Dreval et S. Wolfe, *Development Toward a Repetitive Compact Torus Injector*, IEEE Transactions on Plasma Science, 44 (2016), p. 195–200.

[30] D. W. Peaceman et J. H. H. Rachford, *The Numerical Solution of Parabolic and Elliptic Differential Equations*, Journal of the Society for Industrial and Applied Mathematics, 3 (1955), p. 28–41.

[31] L. J. Perkins, S. K. Ho et J. H. Hammer, *Deep penetration fuelling of reactor-grade tokamak plasmas with accelerated compact toroids*, Nuclear Fusion, 28 (1988), p 1365.

[32] M. Radmilović-Radjenović et B. Radjenović, *The effect of magnetic field on the electrical breakdown characteristics*, Journal of Physics D: Applied Physics, 39 (2006), p 3002.

[33] R. Raman, F. Martin, E. Haddad, M. St-Onge, G. Abel, C. Cote, N. Richard, N. Blanchard, H. H. Mai, B. Quirion, J. L. LaChambre, J. L. Gauvreau, G. W. Pacher, R. DeCoste, P. J. Gierszewski, D. Q. Hwang, A. Hirose, S. Savoie, B. J. LeBlanc, H. McLean, C. Xiao, B. L. Stansfield, A. Cote, D. Michaud et M. Chartre, *Experimental demonstration of tokamak fuelling by compact toroid injection*, Nuclear Fusion, 37 (1997), p 967.

[34] R. Raman, F. Martin, B. Quirion, M. St-Onge, J. L. Lachambre, D. Michaud, B. Sawatzky, J. Thomas, A. Hirose, D. Hwang, N. Richard, C. Côté, G. Abel, D. Pinsonneault, J. L. Gauvreau, B. Stansfield, R. Décoste, A. Côté, W. Zuzak et C. Boucher, *Experimental Demonstration of Nondisruptive, Central Fueling of a Tokamak by Compact Toroid Injection*, Phys. Rev. Lett., 73 (1994), p. 3101–3104.

[35] A. C. Riviere, *Penetration of fast hydrogen atoms into a fusion reactor plasma*, Nuclear Fusion, 11 (1971), p 363.

[36] T. Roche, M. C. Thompson, R. Mendoza, I. Allfrey, E. Garate, J. Romero et J. Douglass, *Enhanced magnetic field probe array for improved excluded flux calculations on the C-2U advanced beam-driven field-reversed configuration plasma experiment*, Review of Scientific Instruments, 87 (2016), p 11D409.

[37] J. A. Rome, J. D. Callen et J. F. Clarke, *Neutral-beam injection into a tokamak, part I: fast-ion spatial distribution for tangential injection*, Nuclear Fusion, 14 (1974), p 141.

[38] L. C. Steinhauer, *Review of field-reversed configurations*, Phys. Plasmas, 18 (2011).

[39] M. SUGIHARA, M. KASAI et T. HIRAOKA, *Ignition Approach by Neutral Beam Injection Heating in Impurity Contaminated Tokamak Reactors*, Journal of Nuclear Science and Technology, 16 (1979), p. 305–315.

[40] Y. Suzuki, T. Hayashi et Y. Kishimoto, *Deceleration mechanism of spheromak-like compact toroid penetrating into magnetized plasmas*, Physics of Plasmas, 7 (2000), p. 5033–5037.

[41] ——, *Effect of magnetic reconnection on CT penetration into magnetized plasmas*, Earth, Planets and Space, 53 (2001), p. 547–551.

[42] Y. Suzuki, T. H. Watanabe, T. Sato et T. Hayashi, *Three dimensional simulation study of spheromak injection into magnetized plasmas*, Nuclear Fusion, 40 (2000), p 277.

[43] D. R. Sweetman, *Ignition condition in Tokamak experiments and role of neutral injection heating*, Nuclear Fusion, 13 (1973), p 157.

[44] T. Takeda et S. Itoh, *Joule Heating in JFT-2*, Japanese Journal of Applied Physics, 10 (1971), p 1083.

[45] M. C. Thompson, J. D. Douglass, P. Feng, K. Knapp, Y. Luo, R. Mendoza, V. Patel, M. Tuszewski et A. D. V. Drie, *Magnetic diagnostic suite of the C-2 field-reversed configuration experiment confinement vessel*, Review of Scientific Instruments, 83 (2012), p 10D709.

[46] M. C. Thompson, H. Gota, S. Putvinski, M. Tuszewski et M. Binderbauer, *Diagnostic suite of the C-2U advanced beam-driven field-reversed configuration plasma experiment*, Review of Scientific Instruments, 87 (2016), p 11D435.

[47] M. Tuszewski, *Field reversed configurations*, Nuclear Fusion, 28 (1988), p 2033.

[48] M. Tuszewski, A. Smirnov, M. C. Thompson, S. Korepanov, T. Akhmetov, A. Ivanov, R. Voskoboynikov, L. Schmitz, D. Barnes, M. W. Binderbauer, R. Brown, D. Q. Bui, R. Clary, K. D. Conroy, B. H. Deng, S. A. Dettrick, J. D. Douglass, E. Garate, F. J. Glass, H. Gota, H. Y. Guo, D. Gupta, S. Gupta, J. S. Kinley, K. Knapp, A. Longman, M. Hollins, X. L. Li, Y. Luo, R. Mendoza, Y. Mok, A. Necas, S. Primavera, E. Ruskov, J. H. Schroeder, L. Sevier, A. Sibley, Y. Song, X. Sun, E. Trask, A. D. Van Drie, J. K. Walters et M. D. Wyman, *Field Reversed Configuration Confinement Enhancement through Edge Biasing and Neutral Beam Injection*, Phys. Rev. Lett., 108 (2012), p 255008.

[49] Z. Wang, P. D. Beinke, C. W. Barnes, M. W. Martin, E. Mignardot, G. A. Wurden, S. C. Hsu, T. P. Intrator et C. P. Munson, *A Penning-assisted subkilovolt coaxial plasma source*, Review of Scientific Instruments, 76 (2005), p 33501.